Research Article | Open Access

Intelligence & Robotics

Shao *et al. Intell. Robot.* **2026**, *6*(4), 985-1014 **DOI:**10.20517/ir.2026.42

Distributed self-localization for dynamic multi-agent systems without a common orientation reference

Die Shao[1], Yunkai Lv[1], Huaicheng Yan[1,2], Penghui Yang[1], Sheng Gao[1]

Keywords:
Distributed self-localization, dynamic multi-agent systems, local reference frames, orientation estimation, relative bearing measurements

Citation: Shao, D.; Lv, Y.; Yan, H.; Yang, P.; Gao, S. Distributed self-localization for dynamic multi-agent systems without a common orientation reference. *Intell. Robot.* **2026**, *6*(4), 985-1014. https://dx.doi.org/10.20517/ir.2026.42

Received: 19 Sep 2026 **First Decision:** 15 Oct 2026 **Revised:** 31 Oct 2026 **Accepted:** 10 Nov 2026 **Published:** 23 Nov 2026

Academic Editor: Jianjun Ni
Copy Editor: Pei-Yun Wang
Production Editor: Pei-Yun Wang

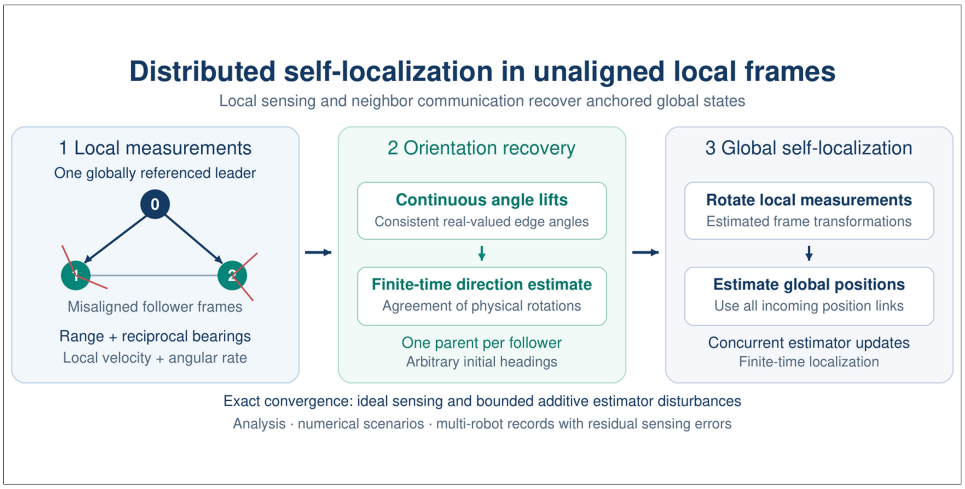

Abstract

This paper investigates distributed self-localization for dynamic multi-agent systems under local perception when a common orientation reference is unavailable. In this setting, inter-agent relative measurements are expressed in different local reference frames and therefore cannot be directly used for global position estimation. To address this issue, a distributed orientation estimator based on local relative bearing measurements with continuous angle lifts on a leader-rooted tree is developed to recover the global orientation of each follower without imposing restrictive initial-orientation conditions. The recovered orientation information is then incorporated into a distributed position estimator to reconstruct the global positions of the followers. The proposed framework also covers the case in which a common orientation reference is available. Rigorous analysis establishes finite-time convergence of both the orientation (modulo 2π) and position estimation errors under the stated exact-measurement and bounded-update-perturbation assumptions. Numerical simulations evaluate the complete continuous-lift estimator, while multi-robot experiments illustrate the practical behavior of the sampled heading-feedback implementation using recorded data.

Check for updates

[1]Key Laboratory of Smart Manufacturing in Energy Chemical Process of the Ministry of Education, East China University of Science and Technology, Shanghai 200237, China.
[2]Faculty of Artificial Intelligence, Shanghai University of Electric Power, Shanghai 200090, China.

Correspondence to: Penghui Yang, Key Laboratory of Smart Manufacturing in Energy Chemical Process of the Ministry of Education, East China University of Science and Technology, Shanghai 200237, China. E-mail: y18253018@mail.ecust.edu.cn

1. INTRODUCTION

Multi-agent systems have been widely investigated because of their broad applications in cooperative control, formation coordination, target tracking, and autonomous navigation[1]. Among the fundamental issues in multi-agent systems, cooperative control[2-4] and localization estimation[5,6] are two closely related topics. Reliable position information is usually a prerequisite for executing coordination tasks. Therefore, developing distributed localization methods with high accuracy and fast convergence is essential for practical multi-agent applications.

Classical localization techniques for multi-agent systems encompass a variety of methods. These include beacon-based localization algorithms with pre-installed anchors[7], concurrent-learning-based relative localization[8], the global positioning system (GPS), simultaneous localization and mapping (SLAM)[9], vision-based localization algorithms[10], among others. Beacon-based global localization requires anchors with known global positions. Conversely, the SLAM and vision-based approaches eliminate the need for an a priori map, instead requiring the scanning and mapping of the target area for the purpose of locating the intelligent agent through matching processes. SLAM and vision-based methods can incur substantial computation and storage costs; the practical burden depends on the sensing configuration and implementation. Although GPS positioning remains a popular method, its accuracy suffers significantly in environments such as indoor spaces or tunnels where GPS signals are obstructed or unavailable.

With the development of onboard sensors such as cameras, lidars, and range sensors, relative measurements among neighboring agents can be obtained more conveniently. This has stimulated increasing interest in distributed localization methods based on local sensing information. For static sensor networks, several distributed localization approaches have been reported. For example, complex-valued Laplacian-based methods have been used for two-dimensional localization problems[5], while barycentric-coordinate-based methods exploit relative distance information to describe inter-node relations[11,12]. Bearing-based localization has also been investigated by using bearing rigidity theory[6].

Bearing rigidity characterizes whether a configuration can be determined from its inter-agent bearings up to translation and scale; it does not require the bearings to remain constant during motion. Nevertheless, maintaining the required geometric constraints can restrict localization in dynamic systems whose configurations vary during motion. Some studies have considered cooperative localization of moving agents without relying on fixed bearing patterns. For instance, cooperative source localization has been studied in[13,14], and bearing-only localization of slowly moving targets has been investigated in[15,16]. Nevertheless, distributed self-localization for dynamic multi-agent systems with time-varying motion remains insufficiently studied.

A major obstacle to distributed self-localization arises when agents do not share a common orientation reference. Let Σ^g denote the global reference frame and Σ^i the local coordinate frame attached to agent i. Because each follower obtains relative measurements in its own local frame, these measurements cannot be directly fused for global position estimation without identifying the orientation relationships among the frames. Recovering the global orientation of each follower from local relative measurements is therefore a prerequisite for distributed self-localization. This issue is particularly relevant in GPS-denied scenarios. For instance, in indoor rescue or disaster-response tasks, a group of mobile robots or drones may need to cooperatively explore an unknown environment using only onboard sensors such as lidars or cameras. Since each agent observes its neighbors with respect to its own heading direction, the absence of a common orientation reference makes conventional localization methods difficult to apply. Existing studies have made some progress on this problem. Ref.[17] studied the self-localization problem of dynamic multi-agent systems with a shared orientation reference. Related orientation-estimation methods were developed in[18,19]. However,

the method in[19] requires the initial orientation angles to belong to a common interval of length less than π, which restricts its applicability in more general cases.

Finite-time orientation estimation has also been studied in[20]. The construction below uses continuously lifted parent–child orientation differences on a selected tree to avoid inconsistent wrapped differences around cycles.

For dynamic multi-agent systems, the localization problem becomes more challenging because the agents keep moving and the estimated positions must be updated in real time. Although finite-time control methods have been successfully applied to prescribed trajectory tracking problems[21,22], they usually assume that the reference information or feedback states are available. This assumption is not satisfied in the localization problem considered here, where the global positions of followers are unknown and need to be recovered from local measurements. For the asymptotic or exponential estimators considered for comparison, exact zero error is approached as time tends to infinity. A finite-time estimator instead provides a settling-time bound under its stated assumptions; its practical speed still depends on the gains, initial errors, and sampling.

Specifically, this paper develops an improved local-measurement-based orientation estimator to recover the global orientation information. With the estimated orientation, a finite-time distributed self-localization scheme under a leader-follower framework is further established to handle systems without bearing rigidity constraints.

The main technical contributions are outlined below.

(i) For agents without a common orientation, a finite-time distributed orientation estimator is constructed. It exploits local relative bearing measurements and continuous angle lifts on a leader-rooted tree and relaxes the initial-orientation restriction required in[19], with convergence understood modulo 2π.

(ii) For moving agents, a finite-time distributed self-localization estimator is constructed. It improves the asymptotic or exponential convergence results in[17-19] by achieving finite-time convergence, with an explicit settling-time bound under the stated assumptions.

2. PRELIMINARIES AND PROBLEM FORMULATION

2.1. Preliminaries

Let $\mathcal{G} = (\mathcal{V}, \mathcal{E})$ describe the directed communication graph among the agents, where $\mathcal{V} = \{0, 1, 2, \ldots, n\}$ is the node set and $\mathcal{E} \subseteq \mathcal{V} \times \mathcal{V}$ is the edge set. For $(j, i) \in \mathcal{E}$ with $0 \le i, j \le n$ and $j \ne i$, agent i can receive information from agent j. The neighbor set of agent i is denoted by $\mathcal{N}_i = \{j \in \mathcal{V} \mid (j, i) \in \mathcal{E}\}$. Since $\mathcal{G}$ is directed, the existence of $(i, j) \in \mathcal{E}$ does not imply that $(j, i) \in \mathcal{E}$ also exists.

A directed graph $\mathcal{G}$ contains a spanning tree if there exists at least one node from which every other node is reachable through directed paths. This node serves as the root of the spanning tree.

For the follower subgraph $\mathcal{G}_0$ consisting of the n followers, define the adjacency matrix as $\mathcal{A} = (a_{ij}) \in \mathbb{R}^{n \times n}$, where $a_{ij} = 1$ if $(j, i) \in \mathcal{E}$, and $a_{ij} = 0$ otherwise, for $1 \le i, j \le n$ and $j \ne i$. The degree matrix is given by $\mathcal{D} = \mathrm{diag}\{d_1, d_2, \ldots, d_n\}$, where $d_i = \Sigma_{j=1}^{n} a_{ij}$. Then the Laplacian matrix of $\mathcal{G}_0$ is defined as $\mathcal{L} = \mathcal{D} - \mathcal{A}$. The information link from the leader to the followers is represented by $\mathcal{B} = \mathrm{diag}\{a_{10}, a_{20}, \ldots, a_{n0}\}$, where $a_{i0} = 1$ if follower i can receive information from the leader, and $a_{i0} = 0$ otherwise.

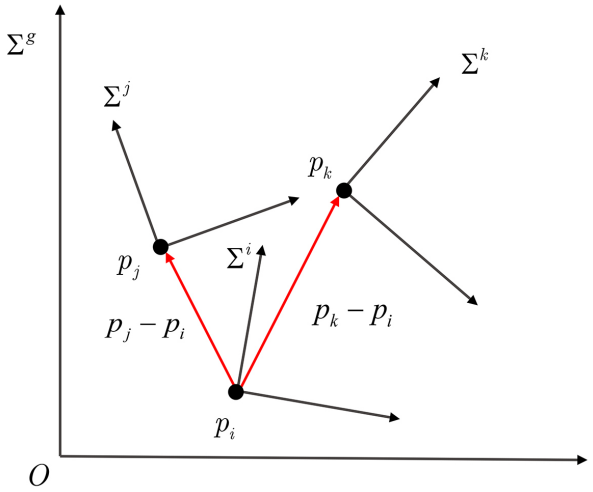

Figure 1. An example of a local reference frame.

As illustrated in Figure 1, each agent is equipped with an individual local reference frame that is generally different from the global frame Σ^g. The local frame of agent i is denoted by Σ^i.

For $z \in \mathbb{R}^2$, sgn(z) acts componentwise. Discontinuous update laws are interpreted in the Filippov sense[23], with the scalar sign replaced at zero by [-1, 1]. The solutions are absolutely continuous, and the differential inequalities below hold almost everywhere. We use $||\cdot||_2$ and $||\cdot||_\infty$ for the Euclidean and maximum norms, respectively.

Moreover, in order to facilitate subsequent analysis, a lemma is given as follows.

Lemma 1([24]; see also[25]). Let $V(t) \geq 0$ be absolutely continuous. Suppose that, whenever $V(t) > 0$,

$$\dot{V}(t) \leq -cV^{\alpha}(t) \quad \textit{almost everywhere}, \qquad c > 0, \quad 0 < \alpha < 1.$$

Then V reaches zero no later than $V(0)^{1-\alpha}/[c(1-\alpha)]$. If the zero set is invariant, V remains zero thereafter. This comparison statement applies to the Filippov solutions used below.

2.2. Problem formulation

Consider a multi-agent system consisting of one leader and n followers, where agent 0 denotes the leader and agents 1, 2, …, n denote the followers. The leader can acquire its global position and orientation through SLAM, GPS, or other localization techniques, whereas the followers cannot directly access their global position information. Each follower can obtain its own motion states through onboard sensors in its local reference frame and exchange information with neighboring agents. Moreover, the relative states of neighboring agents can also be measured in the local reference frame.

Let $p_i \in \mathbb{R}^2$ be the global position of agent i, $\hat{p}_i \in \mathbb{R}^2$ be its estimated global position, and $\tilde{p}_i = \hat{p}_i - p_i$ be the corresponding position estimation error.

Write $\theta_i^c(t)$ for a continuous real lift of the physical heading and $\omega_i = \dot{\theta}_i^c$ for its angular velocity. Rotations depend only on the heading modulo 2π. The physical translational velocity expressed in the body frame is $v_i^i = R_{\theta_i^c}^{\mathrm{T}} \dot{p}_i$; it is not the derivative of the coordinates of the body-frame origin.

The subsequent analysis relies on the following assumptions.

Assumption 1. For each agent, the velocity, acceleration, angular velocity, and angular acceleration are continuous and bounded.

Assumption 2. The directed communication graph admits a leader-rooted spanning tree. For orientation estimation, fix one such tree $\mathcal{T}$ and let $\rho(i)$ denote the unique parent of follower i.

Assumption 3. The relative positions, physical velocities, and angular velocities used by the continuous-time estimators are exact and available without delay. On each edge of $\mathcal{T}$, both reciprocal bearing measurements are available and the two agents do not coincide. The leader supplies $\hat{p}_0 = p_0$, $\dot{\hat{p}}_0 = \dot{p}_0$, $\hat{\theta}_0 = \theta_0^c$, and $\dot{\hat{\theta}}_0 = \omega_0$. The common-orientation case requires only the corresponding position and velocity information. The bounded perturbations below act additively on the update laws; they do not represent arbitrary errors in the raw geometric measurements.

The first two assumptions describe the motion and information structure. Assumption 3 specifies the ideal measurements required for the exact finite-time results; noisy sampled experiments are assessed separately.

The aim of this paper is to construct a distributed self-localization scheme that drives $\hat{\theta}_i$ to θ_i modulo 2π and $\hat{p}_i$ to p_i within a finite time.

3. MAIN RESULTS

In this section, the finite-time self-localization of multi-agent systems is investigated using local perception. Distributed estimation algorithms are constructed, followed by the corresponding convergence analysis.

3.1. Distributed self-localization with global measurements

In this subsection, the common-orientation case is considered. In this case, the locally measured relative position $p_{ji}^{\,i} = p_j^{\,i} - p_i^{\,i}$ in Σ^i coincides with the relative position $p_{ji} = p_j - p_i$ described in Σ^g, namely,

$$p_j^i - p_i^i = p_j - p_i, \tag{1}$$

where $p_j^{\,i}$ and $p_i^{\,i}$ denote the positions of agents j and i described in the local reference frame Σ^i, respectively. Similarly, p_j and p_i denote their positions in the global reference frame Σ^g.

For follower $i \in \{1, 2, \ldots, n\}$, the finite-time distributed self-localization estimator is given by

$$\begin{aligned}\dot{\hat{p}}_i =& \frac{1}{\sum\limits_{j\in\mathcal{N}_i} a_{ij}} \sum_{j\in\mathcal{N}_i} (a_{ij}\dot{\hat{p}}_j) - \frac{1}{\sum\limits_{j\in\mathcal{N}_i} a_{ij}} \sum_{j\in\mathcal{N}_i} a_{ij}(\dot{p}_j - \dot{p}_i) \\ &+ \frac{\eta_1}{\sum\limits_{j\in\mathcal{N}_i} a_{ij}} \operatorname{sgn}\Big(\sum_{j\in\mathcal{N}_i} (a_{ij}(\hat{p}_j - \hat{p}_i - p_{ji}))\Big) \\ &+ \frac{1}{\sum\limits_{j\in\mathcal{N}_i} a_{ij}} \sum_{j\in\mathcal{N}_i} (a_{ij}(\hat{p}_j - \hat{p}_i - p_{ji})) + \varepsilon_i,\end{aligned} \tag{2}$$

where $\dot{\hat{p}}_i$ and $\dot{\hat{p}}_j$ represent the velocity estimates corresponding to agents i and j, respectively, while $\dot{p}_i$ and $\dot{p}_j$ denote their actual velocities. The parameter a_{ij} is the adjacency weight associated with edge (j, i), where $a_{ij} = 1$ when agent i can receive information from agent j, and $a_{ij} = 0$ otherwise. The set $\mathcal{N}_i = \{j \in \mathcal{V} \mid (j, i) \in \mathcal{E}\}$ contains all neighbors of agent i. The term p_{ji} denotes the relative position from agent i to agent j in the global reference frame Σ^g, and $\operatorname{sgn}(\cdot)$ denotes the signum function. The term ε_i represents the bounded

additive update perturbation, satisfying $||\varepsilon_i(t)||_\infty \leq L$, where $L > 0$ is a constant. Let $L_i = \Sigma_{j\in\mathcal{N}_i} a_{ij}L$, where $L_i > 0$. The parameter η_1 is the position-estimation gain and is chosen to satisfy $\eta_1 > \max_{1\leq i\leq n} L_i$.

The complete process of the finite-time distributed self-localization algorithm (2) is given in Algorithm 1.

Algorithm 1 Self-localization estimation of agent i with common orientation

Require: Initial estimate $\hat{p}_i(0)$, exact leader data, and gain $\eta_1 > \max_i L_i$. Derivatives are determined by (2).

1: Measure the velocity $\dot{p}_i$ and the relative position p_{ji}.
2: Transmit $\dot{p}_i$, $\hat{p}_i$, and $\dot{\hat{p}}_i$ to neighboring agents.
3: Receive $\dot{p}_j$, $\hat{p}_j$, and $\dot{\hat{p}}_j$ from neighboring agent j.
4: Update $\dot{\hat{p}}_i$ according to (2).
5: Return to Step 1.

The finite-time convergence property of the proposed estimator is established below.

Theorem 1. For the dynamic multi-agent system with common orientation, suppose that Assumptions 1, 2, and 3 hold. Under the distributed self-localization protocol (2), the position estimate $\hat{p}_i$ reaches the global position p_i in a finite-time interval T_0, namely, $\tilde{p}_i(t) = 0$ for all $t \geq T_0$.

Proof. From the definition of $p_{ji} = p_j - p_i$, it follows that $\dot{p}_{ji} = \dot{p}_j - \dot{p}_i$ and $\dot{\tilde{p}}_i = \dot{\hat{p}}_i - \dot{p}_i$.

Then, the proposed estimation algorithm (2) can be transformed into

$$\sum_{j\in\mathcal{N}_i} a_{ij}(\dot{\tilde{p}}_i - \dot{\tilde{p}}_j) = \eta_1 \operatorname{sgn}\Big(\sum_{j\in\mathcal{N}_i} (a_{ij}(\tilde{p}_j - \tilde{p}_i))\Big) + \sum_{j\in\mathcal{N}_i} (a_{ij}(\tilde{p}_j - \tilde{p}_i)) + \sigma_i, \tag{3}$$

where $\sigma_i = \Sigma_{j\in\mathcal{N}_i} a_{ij}\varepsilon_i$ and $||\sigma_i||_\infty \leq L_i$.

Define

$$s_i = \sum_{j\in\mathcal{N}_i} a_{ij}(\tilde{p}_i - \tilde{p}_j) \in \mathbb{R}^2, \tag{4}$$

then Equation (3) takes the following form

$$\dot{s}_i = -\eta_1 \operatorname{sgn}(s_i) - s_i + \sigma_i. \tag{5}$$

The finite-time convergence of s_i is first established.

Consider the following Lyapunov function,

$$V_i = s_i^{\mathrm{T}} s_i. \tag{6}$$

Differentiating V_i yields

$$\dot{V}_i = 2s_i^{\mathrm{T}}\dot{s}_i = -2\eta_1\|s_i\|_1 - 2\|s_i\|_2^2 + 2s_i^{\mathrm{T}}\sigma_i. \tag{7}$$

By Hölder's inequality, $s_i^{\mathrm{T}}\sigma_i \leq ||s_i||_1||\sigma_i||_\infty \leq L_i||s_i||_1$. Since $||s_i||_1 \geq ||s_i||_2$, Equation (7) gives $\dot{V}_i \leq -2(\eta_1 - L_i)\sqrt{V_i}$ almost everywhere; the scalar sign-based case distinction is unnecessary.

Therefore, Equation (7) can be rewritten as

$$\dot{V}_i \leq -2(\eta_1 - L_i)V_i^{\frac{1}{2}}. \tag{8}$$

Since $\eta_1 - L_i > 0$ and $V_i \geq 0$, Lemma 1 implies that s_i reaches zero within a finite-time interval T_i. Therefore,

$$V_i^{\frac{1}{2}} \leq \max\{0, \sqrt{V_i(0)} - (\eta_1 - L_i)t\}. \tag{9}$$

The finite convergence time T_i satisfies

$$T_i \leq \frac{V_i^{\frac{1}{2}}(0)}{\eta_1 - L_i}, \tag{10}$$

where $V_i(0) = s_i^{\mathrm{T}}(0)s_i(0)$.

The same inequality prevents V_i from increasing away from zero after it first reaches zero. Thus, the zero set is invariant despite the bounded additive perturbation under the Filippov interpretation.

Therefore, one can conclude that s_i will converge to zero when $t \geq T_0 = \max(T_1, T_2, \ldots, T_n)$.

Next, we will prove the finite-time convergence of $\tilde{p}_i$.

From Equation (4), the following compact representation is obtained:

$$S = [(\mathcal{L} + \mathcal{B}) \otimes I_2](\tilde{P} - \tilde{P}_0), \tag{11}$$

where $S = \mathrm{col}(s_1, s_2, \ldots, s_n) \in \mathbb{R}^{2n}$, $\tilde{P} = \mathrm{col}(\tilde{p}_1, \tilde{p}_2, \ldots, \tilde{p}_n) \in \mathbb{R}^{2n}$, and $\tilde{P}_0 = \mathbf{1}_n \otimes \tilde{p}_0 \in \mathbb{R}^{2n}$. The matrix $\mathcal{B} = \mathrm{diag}\{a_{10}, a_{20}, \ldots, a_{n0}\}$ characterizes the leader-follower information links, where $a_{i0} = 1$ if follower i receives information from the leader, and $a_{i0} = 0$ otherwise. Moreover, $\mathcal{L} = \mathcal{D} - \mathcal{A}$ is the Laplacian matrix of the follower subgraph, where $\mathcal{D} = \mathrm{diag}\{d_1, d_2, \ldots, d_n\}$, $d_i = \Sigma_{j=1}{}^{n} a_{ij}$, and $\mathcal{A} = (a_{ij}) \in \mathbb{R}^{n \times n}$ with $a_{ij} = 1$ if $(j, i) \in \mathcal{E}$ and $a_{ij} = 0$ otherwise.

Equation (11) can be reformulated as

$$\mathrm{col}(0_2, S) = \left(\begin{bmatrix} 0 & \mathbf{0}_n^{\mathrm{T}} \\ -b & \mathcal{L} + \mathcal{B} \end{bmatrix} \otimes I_2 \right) \mathrm{col}(\tilde{p}_0, \tilde{P}), \tag{12}$$

where $\mathbf{0}_n$ denotes n-dimensional zero vector, $0_2 \in \mathbb{R}^2$, and $b = \mathcal{B}\mathbf{1}_n \in \mathbb{R}^n$.

Let $\mathcal{L}_0 = \begin{bmatrix} 0 & \mathbf{0}_n^{\mathrm{T}} \\ -b & \mathcal{L} + \mathcal{B} \end{bmatrix}$. Since $\tilde{p}_0 \equiv 0$, (12) becomes a linear algebraic relation whose variables are $\tilde{p}_1, \tilde{p}_2, \ldots, \tilde{p}_n$. By Assumption 2, the directed graph admits a leader-rooted spanning tree. Therefore, the grounded Laplacian $\mathcal{L} + \mathcal{B}$ is nonsingular. Equivalently, the augmented Laplacian $\mathcal{L}_0$ has rank n and nullspace span$\{\mathbf{1}_{n+1}\}$; its planar extension has nullspace $\mathbf{1}_{n+1} \otimes \mathbb{R}^2$. Fixing the leader error to zero removes this two-dimensional translation freedom. Consequently, when $S = \mathbf{0}_{2n}$, the only solution to (12) is $\tilde{P} = \mathbf{0}_{2n}$. Therefore, $\tilde{P}$ reaches zero for $t \geq T_0$.

Since $\tilde{p}_i = \hat{p}_i - p_i$, it follows that the position estimate $\hat{p}_i$ reaches the actual global position p_i for $t \geq T_0$.

This completes the proof.

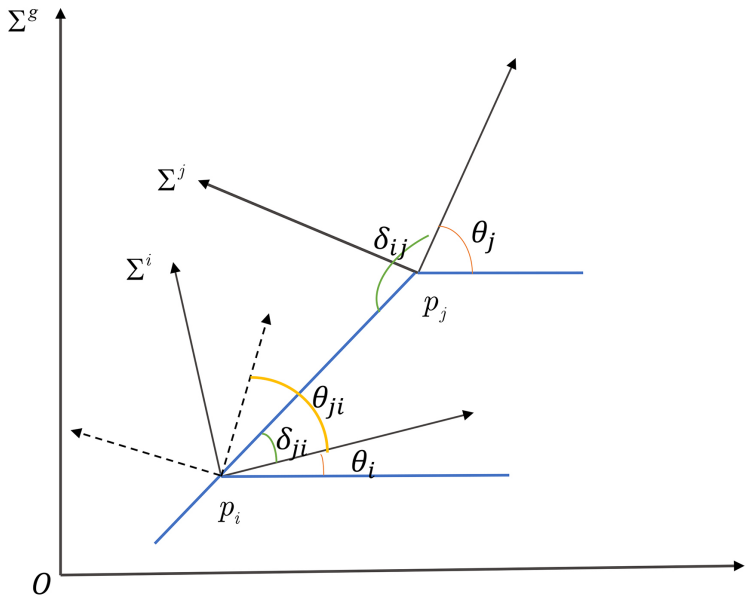

Figure 2. The relationships among orientations.

Remark 1. Equation (2) is designed to refine the estimated position by leveraging the discrepancy between the observed and the predicted relative information. Consequently, this process enables the transformation of the estimated position's convergence into the convergence of the estimation error. This ensures that the follower's estimation error aligns with that of the leader. The leader's estimation error is considered to be zero, given the leader's ability to accurately determine its own position.

Remark 2. For static systems, Algorithm 1 remains valid by setting the relative velocity term $\dot{p}_j$ - $\dot{p}_i$ in (2) to zero.

3.2. Distributed self-localization with local measurements

The non-common-orientation setting is considered, as illustrated in Figure 1. In this situation, each agent obtains relative position and velocity information only with respect to its own local reference frame, and hence Equation (1) no longer holds. Therefore, global orientation estimation is required before constructing the position estimation algorithm for the followers.

Figure 2 depicts the geometric relationship between local bearing measurements and agent orientations. In the local frame Σ^i, follower agent i measures $\delta_{ji} \in [0, 2\pi)$. Meanwhile, agent i receives $\delta_{ij} \in [0, 2\pi)$ from agent j through communication.

According to the geometric relationship shown in Figure 2, the global relative orientation $\theta_{ji} \in [0, 2\pi)$ of agents i and j is obtained from the local relative bearing angles as

$$\theta_{ji} = (\delta_{ji} - \delta_{ij} + \pi) \bmod (2\pi), \tag{13}$$

where θ_i and θ_j are the global orientations corresponding to agents i and j, respectively.

Only the value at initialization is wrapped. On each selected tree edge $j = \rho(i)$, propagate a continuous lift by

$$\bar{\theta}_{ji}(t) = \theta_{ji}(0) + \int_0^t [\omega_j(\tau) - \omega_i(\tau)]\, d\tau.$$

Reciprocal bearings initialize this lift. After initialization, the orientation update propagates it using angular-velocity differences; subsequent bearing measurements are not used to correct the propagated orientation. Set $a_{ij}^{\theta} = 1$ for $j = \rho(i)$ and $a_{ij}^{\theta} = 0$ otherwise, so that $\Sigma_{j\in\mathcal{N}_i} a_{ij}^{\theta} = 1$. Use these weights only in the orientation estimator; the position estimator retains all original edges. The continuous lift prevents branch-cut jumps, and the single-parent tree prevents inconsistent lifts along cycles or multiple paths. No restriction on the initial physical headings or on $\hat{\theta}_i(0)$ is imposed.

To estimate the global position of agent i after recovering its global orientation, two finite-time distributed estimators are constructed, including an orientation estimator and a self-localization estimator. Their update laws are given as follows.

$$\begin{aligned}\dot{\hat{\theta}}_i =& \frac{1}{\sum\limits_{j\in\mathcal{N}_i} a_{ij}^{\theta}} \sum_{j\in\mathcal{N}_i} (a_{ij}^{\theta}\dot{\hat{\theta}}_j) - \frac{1}{\sum\limits_{j\in\mathcal{N}_i} a_{ij}^{\theta}} \sum_{j\in\mathcal{N}_i} a_{ij}^{\theta}(\omega_j - \omega_i) \\ &+ \frac{\eta_2}{\sum\limits_{j\in\mathcal{N}_i} a_{ij}^{\theta}} \operatorname{sgn}\Big(\sum_{j\in\mathcal{N}_i} (a_{ij}^{\theta}(\hat{\theta}_j - \hat{\theta}_i - \bar{\theta}_{ji}))\Big) \\ &+ \frac{1}{\sum\limits_{j\in\mathcal{N}_i} a_{ij}^{\theta}} \sum_{j\in\mathcal{N}_i} (a_{ij}^{\theta}(\hat{\theta}_j - \hat{\theta}_i - \bar{\theta}_{ji})) + \varepsilon_i^{\theta},\end{aligned} \tag{14}$$

$$\begin{aligned}\dot{\hat{p}}_i =& \frac{1}{\sum\limits_{j\in\mathcal{N}_i} a_{ij}} \sum_{j\in\mathcal{N}_i} (a_{ij}\dot{\hat{p}}_j) - \frac{1}{\sum\limits_{j\in\mathcal{N}_i} a_{ij}} \sum_{j\in\mathcal{N}_i} a_{ij}(R_{\hat{\theta}_j} v_j^j - R_{\hat{\theta}_i} v_i^i) \\ &+ \frac{\eta_3}{\sum\limits_{j\in\mathcal{N}_i} a_{ij}} \operatorname{sgn}\Big[\sum_{j\in\mathcal{N}_i} (a_{ij}(\hat{p}_j - \hat{p}_i - R_{\hat{\theta}_i} p_{ji}^i))\Big] \\ &+ \frac{1}{\sum\limits_{j\in\mathcal{N}_i} a_{ij}} \sum_{j\in\mathcal{N}_i} (a_{ij}(\hat{p}_j - \hat{p}_i - R_{\hat{\theta}_i} p_{ji}^i)) + \varepsilon_i^{p},\end{aligned} \tag{15}$$

where ω_i, $\hat{\theta}_i$ and $\dot{\hat{\theta}}_i$ denote the angular velocity, the estimated global orientation, and the estimated orientation velocity of agent i, respectively. The terms v_j^j and v_i^i are the velocities of agents j and i expressed in their corresponding local reference frames. The rotation matrix associated with the angle θ is defined as $R_\theta = \begin{bmatrix}\cos\theta & -\sin\theta \\ \sin\theta & \cos\theta\end{bmatrix}$. Similarly, ε_i^{θ} and ε_i^{p} denote the bounded additive update perturbations. They satisfy $|\varepsilon_i^{\theta}(t)| \le L_i^{\theta}$ and $||\varepsilon_i^{p}(t)||_\infty \le L_i^{p}$, where $L_i^{\theta} > 0$ and $L_i^{p} > 0$ are bounded constants. Let $L^{\theta} = \max_i L_i^{\theta}$ and $L^{p} = \max_i v_i L_i^{p}$, where $v_i = \Sigma_{j\in\mathcal{N}_i} a_{ij} = d_i + a_{i0}$. The gains η_2 and η_3 are selected such that $\eta_2 > L^{\theta}$ and $\eta_3 > L^{p}$, respectively.

The procedures for the finite-time distributed estimation methods (14) and (15) are described in Algorithm 2.

Algorithm 2 Self-localization of agent i without common orientation

Require: Initial estimates $\hat{p}_i(0)$ and $\hat{\theta}_i(0)$ are randomly given. Fix $\rho(i)$, initialize $\bar{\theta}_{\rho(i)i}(0) = \theta_{\rho(i)i}(0)$ using (13), and use the stated gains and exact leader data. Derivatives follow (14)–(15).

1: Measure the relative position p_{ji}^i, relative bearing angle δ_{ji}, velocity v_i^i, and angular velocity ω_i in its own reference frame Σ^i.
2: Transmit v_i^i, $\hat{p}_i$, $\hat{\theta}_i$, $\dot{\hat{p}}_i$, $\dot{\hat{\theta}}_i$, δ_{ji}, and ω_i to neighboring agents.
3: Receive the neighbor estimates and velocities needed in (15), and the parent's reciprocal bearing, angular velocity, and estimated orientation derivative.
4: Propagate $\bar{\theta}_{\rho(i)i}$ continuously with $\dot{\bar{\theta}}_{\rho(i)i} = \omega_{\rho(i)} - \omega_i$; do not wrap it again.
5: Update $\dot{\hat{\theta}}_i$ according to (14).
6: Update $\dot{\hat{p}}_i$ according to (15).
7: Return to Step 1.

The finite-time convergence of the distributed self-localization algorithms in (13)-(15) is established in the following theorem.

Theorem 2. For the multi-agent system without common orientation, suppose that Assumptions 1, 2, and 3 are satisfied. Under the distributed self-localization algorithms (13)-(15), the estimated global orientation $\hat{\theta}_i$ reaches the actual global orientation θ_i modulo 2π for $t \geq T_\theta$, and the position estimate $\hat{p}_i$ reaches the actual global position p_i for $t \geq T_\theta + T_p$, with finite bounds specified below.

Proof. Define virtual real headings recursively on $\mathcal{T}$ by $\psi_0 = \theta_0^c$ and $\psi_i = \psi_{\rho(i)} - \bar{\theta}_{\rho(i)i}$. At initialization, each wrapped edge measurement differs from the true real orientation difference by an integer multiple of 2π. Integration of the exact angular velocities preserves that integer. Induction along the tree therefore gives $\psi_i = \theta_i^c + 2\pi k_i$, $k_i \in \mathbb{Z}$, and $\dot{\psi}_i = \omega_i$. Hence $R_{\psi i} = R_{\theta_i}$ for all time, although the real representatives need not be equal.

Let $e_i = \hat{\theta}_i - \psi_i$, $e_0 = 0$, and $q_i = e_i - e_{\rho(i)}$. Substituting the single-parent weights into (14) gives

$$\dot{q}_i = -\eta_2 \operatorname{sgn}(q_i) - q_i + \varepsilon_i^\theta.$$

For $W_i = q_i^2$, the almost-everywhere inequality $\dot{W}_i \leq -2(\eta_2 - L_i^\theta)\sqrt{W_i}$ follows. Lemma 1 and zero-set invariance yield

$$T_\theta \leq \max_i \frac{|q_i(0)|}{\eta_2 - L_i^\theta}.$$

For $t \geq T_\theta$, every $q_i = 0$; recursion from $e_0 = 0$ then gives $e_i = 0$. Since $\psi_i = \theta_i^c + 2\pi k_i$ and $e_i = \hat{\theta}_i - \psi_i$, the physical circular orientation error satisfies $e_{i,\mathrm{circ}}{}^\theta = |\mathrm{atan2}(\sin(\hat{\theta}_i - \theta_i^c), \cos(\hat{\theta}_i - \theta_i^c))| = |\mathrm{atan2}(\sin e_i, \cos e_i)|$. Therefore, for $t \geq T_\theta$, $e_{i,\mathrm{circ}}{}^\theta = 0$ and $R_{\hat{\theta}_i} = R_{\theta_i^c} = R_{\theta_i}$. This proves convergence of physical orientations modulo 2π without identifying inconsistent wrapped measurements with ordinary real differences.

Before T_θ, bounded physical velocities imply bounded relative positions on every finite interval, and rotation matrices have norm one. Multiplying the stacked position law by $\mathcal{L} + \mathcal{B}$ yields an explicit differential inclusion because this grounded Laplacian is nonsingular. Its right-hand side grows at most linearly with the stacked position estimate, with bounded inputs and sign terms. Gronwall's inequality therefore excludes finite escape and ensures that $\hat{p}_i(T_\theta)$ is finite. For $t \geq T_\theta$, the equality of rotation matrices reduces (15) to the following position-estimation law:

$$\begin{aligned}\dot{\hat{p}}_i =& \frac{1}{\sum_{j\in\mathcal{N}_i} a_{ij}} \sum_{j\in\mathcal{N}_i} (a_{ij}\dot{\hat{p}}_j) - \frac{1}{\sum_{j\in\mathcal{N}_i} a_{ij}} \sum_{j\in\mathcal{N}_i} a_{ij}(R_{\theta_j} v_j^j - R_{\theta_i} v_i^i) \\ &+ \frac{\eta_3}{\sum_{j\in\mathcal{N}_i} a_{ij}} \operatorname{sgn}\Big[\sum_{j\in\mathcal{N}_i} (a_{ij}(\hat{p}_j - \hat{p}_i - R_{\theta_i} p_{ji}^i))\Big] \\ &+ \frac{1}{\sum_{j\in\mathcal{N}_i} a_{ij}} \sum_{j\in\mathcal{N}_i} (a_{ij}(\hat{p}_j - \hat{p}_i - R_{\theta_i} p_{ji}^i)) + \varepsilon_i^p.\end{aligned} \tag{16}$$

According to the coordinate transformation, one has $R_{\theta_j} v_j^j - R_{\theta_i} v_i^i = \dot{p}_j - \dot{p}_i = \dot{p}_{ji}$ and $R_{\theta_i} p_{ji}^i = p_{ji}$. Then, an equivalent representation of (16) is obtained as

$$\begin{aligned}\dot{\hat{p}}_i =& \frac{1}{\sum_{j\in\mathcal{N}_i} a_{ij}} \sum_{j\in\mathcal{N}_i} (a_{ij}\dot{\hat{p}}_j) - \frac{1}{\sum_{j\in\mathcal{N}_i} a_{ij}} \sum_{j\in\mathcal{N}_i} (a_{ij}\dot{p}_{ji}) \\ &+ \frac{\eta_3}{\sum_{j\in\mathcal{N}_i} a_{ij}} \operatorname{sgn}\Big(\sum_{j\in\mathcal{N}_i} (a_{ij}(\hat{p}_j - \hat{p}_i - p_{ji}))\Big) \\ &+ \frac{1}{\sum_{j\in\mathcal{N}_i} a_{ij}} \sum_{j\in\mathcal{N}_i} (a_{ij}(\hat{p}_j - \hat{p}_i - p_{ji})) + \varepsilon_i^p.\end{aligned} \tag{17}$$

By applying Theorem 1 from time T_θ, the position-estimation error reaches zero within finite time. In particular, with $s_i^p = \Sigma_{j\in\mathcal{N}_i} a_{ij}(\tilde{p}_i - \tilde{p}_j)$, one may use $T_p \le \max_i \|s_i^p(T_\theta)\|_2/(\eta_3 - v_i L_i^p)$. Specifically, $\hat{p}_i$ reaches p_i for all $t \ge T_\theta + T_p$.

This completes the proof.

Remark 3. The convergence analysis of orientation estimation and position estimation is presented sequentially for clarity. In a practical implementation, the two estimators are executed concurrently in a distributed manner.

Remark 4. With a common orientation, (2) uses globally aligned relative positions and velocities directly. Without it, (14) adds reciprocal bearing and angular-velocity exchange, a maintained continuous angle lift, and an orientation transient before the position bound applies. In return, (15) can fuse measurements from different local frames without initial heading alignment. Both cases use a leader reference and relative position information; the latter method is not a bearing-only position localizer. The tree construction avoids cycle inconsistencies but does not exploit redundant orientation edges. Exact finite-time convergence applies to the continuous-time model with the exact angular velocities specified in Assumption 3. Angular-rate bias in the propagated lift produces accumulated drift. To quantify this effect, consider measured rates $\omega_i^{\mathrm{m}} = \omega_i + \beta_i$ with constant biases and exact bearing initialization, and use the same measured rates in the lift and the feedforward term of (14). The resulting lift and virtual-heading errors satisfy

$$\Delta\bar{\theta}_{ji}(t) = (\beta_j - \beta_i)t, \qquad \Delta\psi_i(t) = (\beta_i - \beta_0)t.$$

Here $\Delta\bar{\theta}_{ji}$ and $\Delta\psi_i$ denote deviations from their exact-rate counterparts. Edge errors are inherited by downstream followers; for the node-wise biases above, their sum along the leader–follower path telescopes to the stated $\Delta\psi_i$. Even when the internal tree errors q_i vanish, the physical orientation contains this drift. Its circular error is $|\mathrm{atan2}(\sin\Delta\psi_i, \cos\Delta\psi_i)|$, which is bounded by π but need not remain small. For any local vector $z \in \mathbb{R}^2$, the associated rotation mismatch then obeys

$$\left\|(R_{\hat{\theta}_i} - R_{\theta_i^c})z\right\|_2 = 2\left|\sin(\Delta\psi_i/2)\right| \|z\|_2 \le \min\{2, |\beta_i - \beta_0|t\} \|z\|_2.$$

Taking $z = p_{ji}{}^i$ or $z = vi^i$ quantifies the geometric perturbations entering the position estimator (15). Thus, Theorem 2 does not provide exact recovery or a uniform small-error bound for biased angular-rate measurements. Sensor noise, sampling, and numerical sign regularization also affect practical accuracy; bounded residual errors under these measurement and implementation effects are not established by the present analysis.

4. SIMULATION AND EXPERIMENT

4.1. Simulation

This section validates the proposed finite-time distributed self-localization algorithms using a finite-time path tracking task, in which the simulated controller relies on the estimated position.

The information exchange structure is depicted in Figure 3, where the red star represents the leader agent and the remaining five nodes represent the followers. The topology mirrors that used in the simulation presented in[17] for comparative purposes. All edges have unit weights, with parent nodes $(\rho(1), \rho(2), \rho(3), \rho(4), \rho(5)) = (0, 0, 0, 3, 4)$, so $v_i = 1$ in Scenarios 1-3. The simulations implement both the sign and linear residual terms of the proposed estimators. In Scenario 3, reciprocal bearings initialize the tree-edge angle lifts,

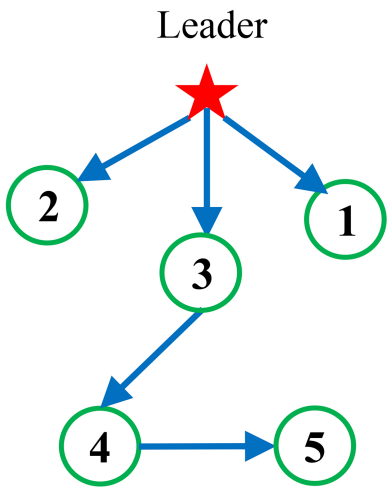

Figure 3. Communication topology of the multi-agent system.

which are then propagated using exact angular-velocity differences. The integration step and disturbance-refresh interval are $h = 10^{-3}$ s. The estimator sign inclusions are solved by implicit Euler with componentwise soft thresholding. Local relative measurements and angular rates are exact; the specified perturbations enter the estimator updates. One position-perturbation sample is applied to both Cartesian components of each follower, with independent draws across followers and update intervals. The random seeds are 1101, 1102, and 1103, respectively. The leader follows $p_0(t) = (0.1t, 0.2t)^{\mathsf{T}}$ m, and the follower translational velocities are initially zero.

Three path-tracking cases are considered: switching static targets with common orientation, moving targets with common orientation, and moving targets without common orientation. The localization estimates provide feedback to the tracking controllers. In the first two cases, orientation is common and known; no orientation estimator is needed, and $\varepsilon_i^{\theta} = 0$.

4.1.1. Scenario 1. Static target with common orientation

The initial positions, initial target positions, and changed target positions at $t = t_{\mathrm{sw}} = 10$ s are set as

$$\begin{aligned}\mathcal{P}_0 &= \{(1,5),(3,3),(4,2),(7,6),(2,3)\},\\ \mathcal{P}_d(0) &= \{(4,4),(5,3),(2,3),(2,4),(3,3.5)\},\\ \mathcal{P}_d(t_{\mathrm{sw}}) &= \{(17,15),(13,15),(15,13),(15,17),(15,15)\}.\end{aligned}$$

The position gain is $\eta_1 = 12$. Each additive position-update component is uniformly distributed on [-1, 1] m/s, giving $L = 1$ and $L_i = v_i L = 1$. Hence $\eta_1 = 12 > \max_i L_i = 1$, satisfying the gain condition of Theorem 1. The initial follower position estimates are {(2,5), (2,2), (3,2), (5,5), (2,2)} m, and the leader supplies its exact position reference. The tracking gains are $\alpha_i = 3$ and $\beta_i = 2$ for every follower.

Consider the double-integrator model and the control law as follows.

$$\dot{p}_i = v_i, \qquad \dot{v}_i = u_i, \qquad u_i = -\alpha \operatorname{sgn}\left[\dot{p}_i + \beta \operatorname{sig}^{1/2}(\hat{p}_i - p_i^*)\right], \tag{18}$$

where α and β denote positive control gains satisfying $\alpha > \frac{1}{2}\beta^2$, and p_i^* denotes the target position of agent i. The gains in each tracking law may differ across followers; their individual values are denoted by α_i and β_i.

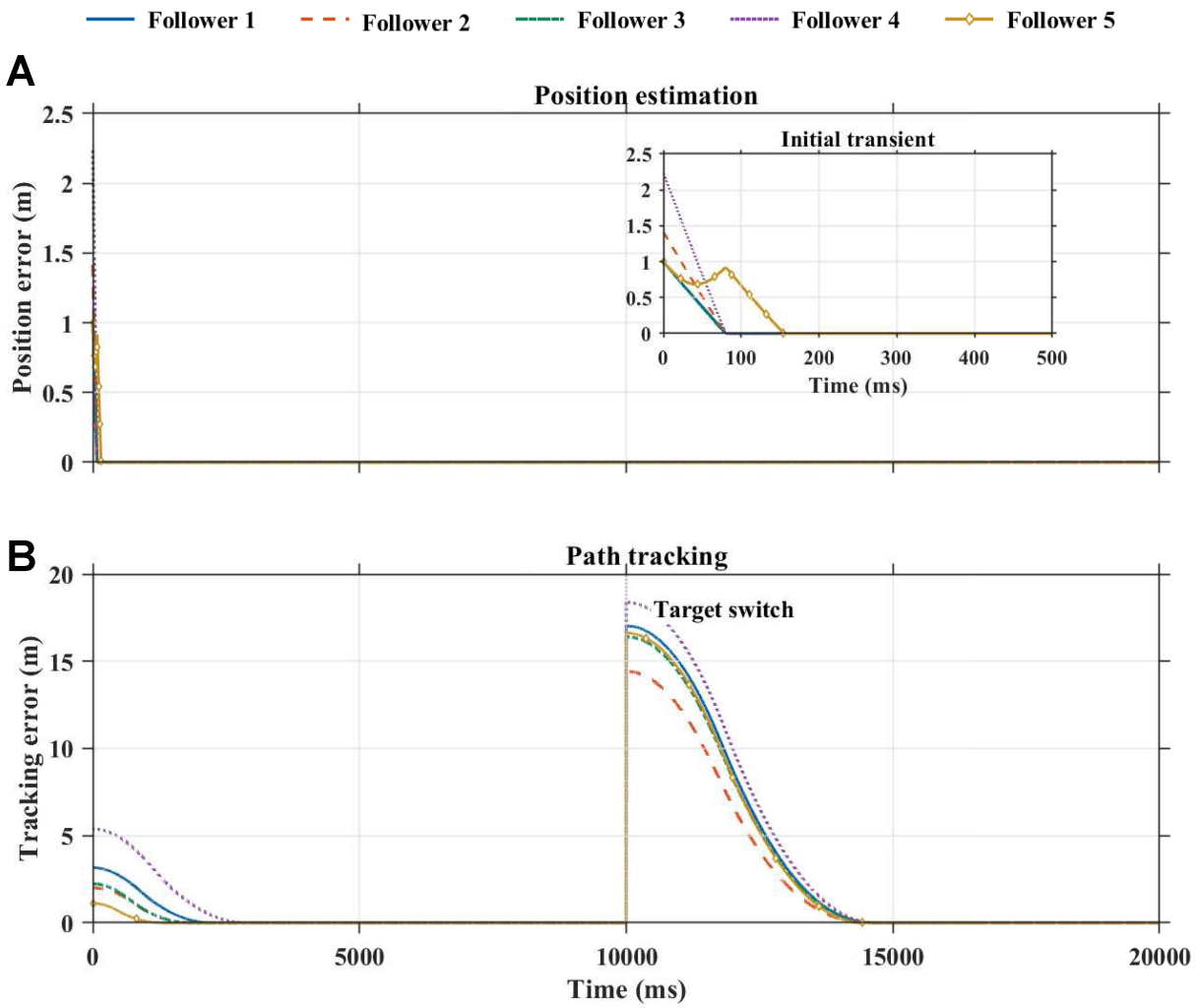

Figure 4. Common orientation and switching static targets: (A) position-estimation errors; (B) path-tracking errors. The inset resolves the initial localization transient, and the vertical dotted line marks the target switch. Colours and line styles identify followers 1-5 consistently between panels; time is in milliseconds.

The estimated position $\hat{p}_i$ is adopted as the feedback information for path tracking. After Algorithm 1 is applied, Figure 4A presents the position-estimation errors, and Figure 4B presents the path-tracking errors. Matching colours and line styles identify the five followers across the two panels. The tracking error is defined by the Euclidean distance between the actual position and the target position, i.e., $||p_i - p_i^*||$.

On the saved 1 ms grid, all position errors remain below 10^{-7} m from $t = 0.155$ s, compared with the conservative bound $T_0 \leq 0.182$ s from Theorem 1. The target switch at $t = 10$ s produces a new path-tracking transient while the position-estimation errors remain below this tolerance. Figure 5 compares the actual trajectories with the estimated trajectories, showing that Algorithm 1 achieves fast and accurate position estimation.

The time axis in Figure 4 is in milliseconds: 10^4 ms = 10 s. The target switch at $t = 10$ s produces tracking-error peaks of up to approximately 18.38 m, whereas the position-estimation errors remain small.

For comparison, the velocity-fed linear position-estimation structure in[17] is evaluated on the same simulated motions. With $\check{p}_i$ denoting the comparison estimate, the implemented update is

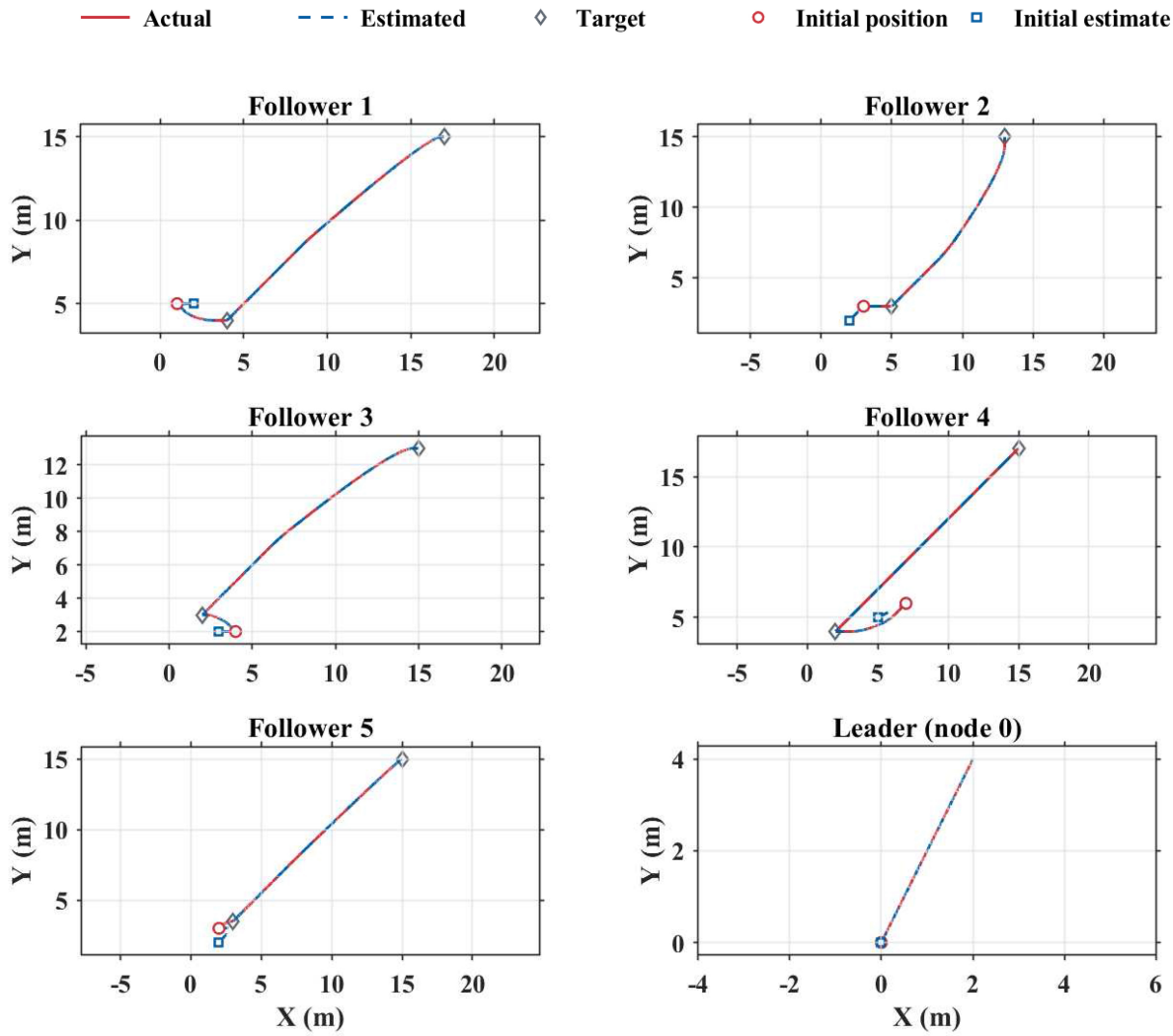

Figure 5. The estimated trajectories with common orientation and static targets.

$$\dot{\check{p}}_i = v_i + k_p\left(\check{p}_{\rho(i)} - \check{p}_i - p_{\rho(i)i}\right) + \varepsilon_i, \qquad k_p = 3.$$

The measured own velocity replaces the single-integrator input in the reference estimator. Both observers use identical initial estimates, leader references, local measurements, integration steps, and position-update perturbations. Figure 6 presents one follower per panel: blue curves with hollow circles denote the proposed estimator, and orange curves with hollow squares denote the linear comparison. The insets show the shorter initial localization transient of the proposed estimator in this run.

4.1.2. Scenario 2. Dynamic target with common orientation

In this part, the target positions of the follower agents are time-varying. The initial positions and target paths are set as

$$\begin{aligned}\mathcal{P}_0 =&\{(3,4),(5,3),(5,4),(7,5),(6,4)\},\\ \mathcal{P}^*(t) =&\{(1+2t,5+\cos(1+2t)),(3+t,3+\cos(3+t)),\\ &(4+3t,2+2\cos(4+3t)),(2+t,3+\cos(2t+4)),\\ &(7-1.1t,6-1.1t)\}.\end{aligned} \tag{19}$$

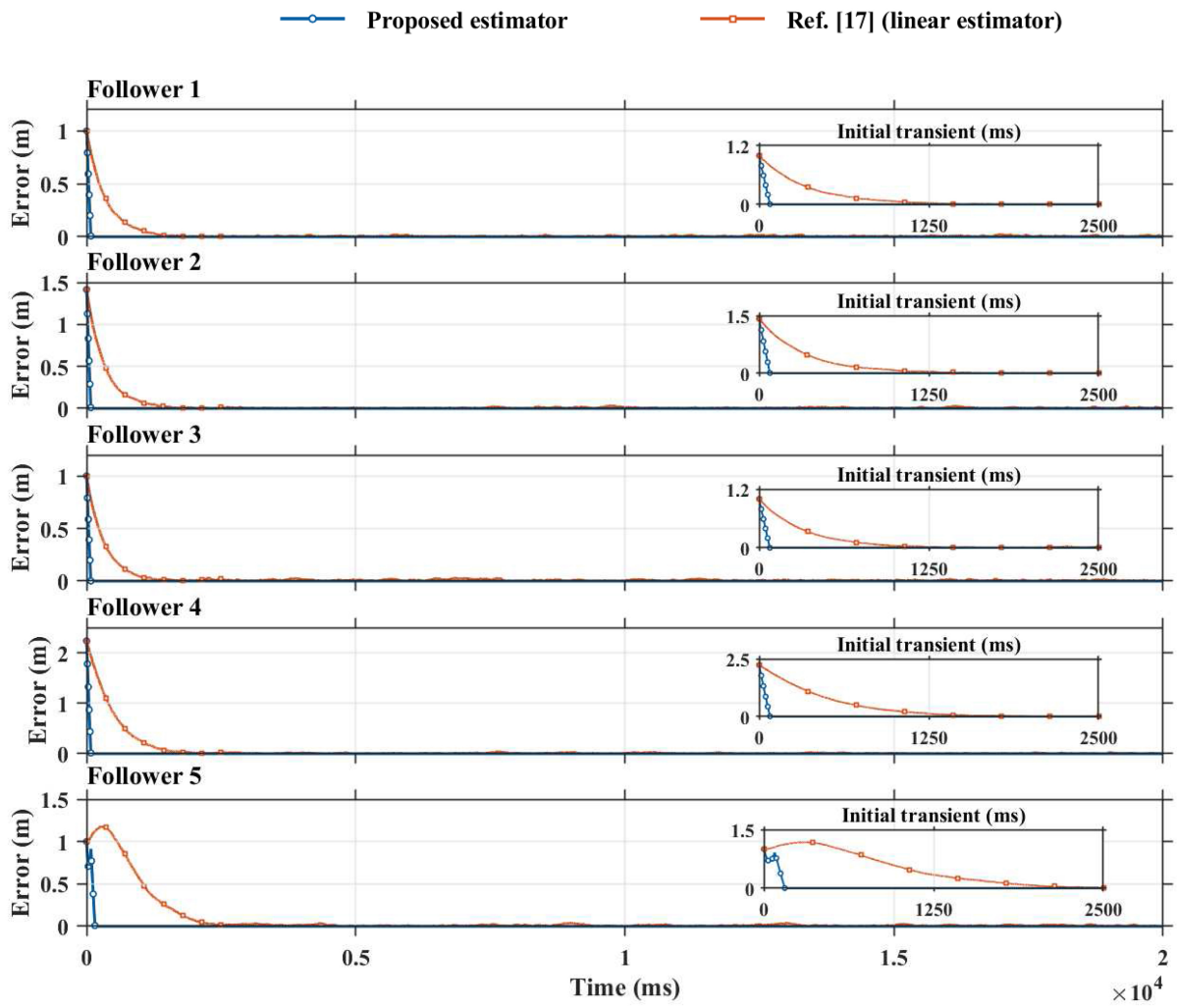

Figure 6. Position-error comparison with common orientation and switching static targets. Each panel represents one follower. Blue circles: proposed estimator; orange squares: velocity-fed linear comparison based on[17]. Main panels: 0-20,000 ms; initial-transient insets: 0-2,500 ms.

The position gain is $\eta_1 = 10$. Each position-update component is uniformly distributed on [-1, 1] m/s, so $L = 1$, $L_i = v_i L = 1$, and $\eta_1 = 10 > \max_i L_i = 1$, as required by Theorem 1. The initial position estimates are the same as in Scenario 1. The tracking gains are $(\alpha_i)_{i=1}^{5} = (6, 6, 24, 6, 2)$ and $(\beta_i)_{i=1}^{5} = (3, 3, 3, 3, 1)$.

The adopted controller is shown below

$$u_i = -\alpha \operatorname{sgn}\left[\dot{p}_i - \dot{p}_i^* + \beta \operatorname{sig}^{\frac{1}{2}}(\hat{p}_i - p_i^*)\right], \tag{20}$$

where $\alpha > \frac{1}{2}\beta^2$, and $\operatorname{sig}^{\gamma}(x) = |x|^{\gamma}\operatorname{sgn}(x)$.

In this scenario, the leader follows a straight path, while the followers move along sinusoidal or linear trajectories according to (20). Algorithm 1 is applied. Figure 7A displays the position-estimation errors, and Figure 7B displays the path-tracking errors, with consistent follower colours and line styles. All position errors remain below 10^{-7} m from $t = 0.265$ s on the saved grid; the conservative bound from Theorem 1 is $T_0 \leq 0.352$ s. Figure 8 compares the actual and estimated trajectories.

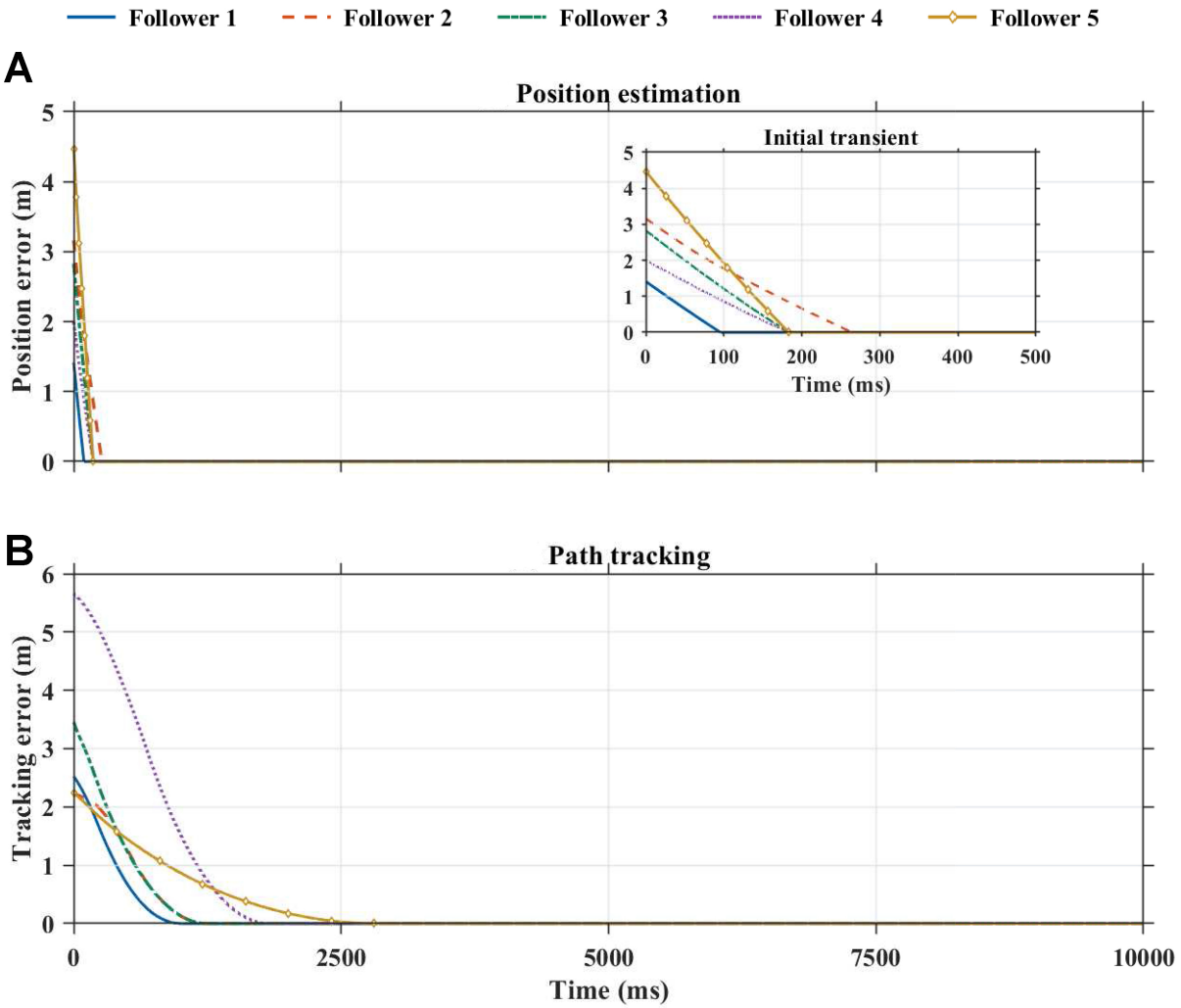

Figure 7. Common orientation and moving targets: (A) position-estimation errors; (B) path-tracking errors. The inset resolves the initial localization transient. Colours and line styles identify followers 1-5 consistently between panels; time is in milliseconds.

Figure 9 compares the proposed estimator with the same velocity-fed linear estimator based on[17], now using $k_p = 7$. Both observers use the same motion and measurement records, initial estimates, and additive perturbations. Each panel shows one follower, with blue circular markers for the proposed estimator and orange square markers for the linear comparison. The full record and initial-transient insets show rapid position recovery by the proposed estimator and the longer transient of the linear comparison in this run.

For follower 5 in (19), the target coordinates cross zero at $t = 70/11$ s and $t = 60/11$ s, respectively, and the target at 10 s is (-4, -5) m. The actual and estimated trajectories of follower 5 in Figure 8 extend into the negative-coordinate region and closely overlap after the initial estimation transient.

4.1.3. Scenario 3. Dynamic target without common orientation

In this part, the initial positions and target paths are set as

$$\begin{aligned}\mathcal{P}_0 =&\{(3,4),(5,3),(5,4),(7,5),(6,4)\},\\ \mathcal{P}^*(t) =&\{(1+2t,5+\cos(1+2t)),(3+0.2t,3+\cos(3+0.2t)),\\ &(4+0.5t,2+\cos(4+0.5t)),(2+0.8t,3+\cos(2t+1.6)),\\ &(7-0.55t,6-0.55t)\}.\end{aligned} \tag{21}$$

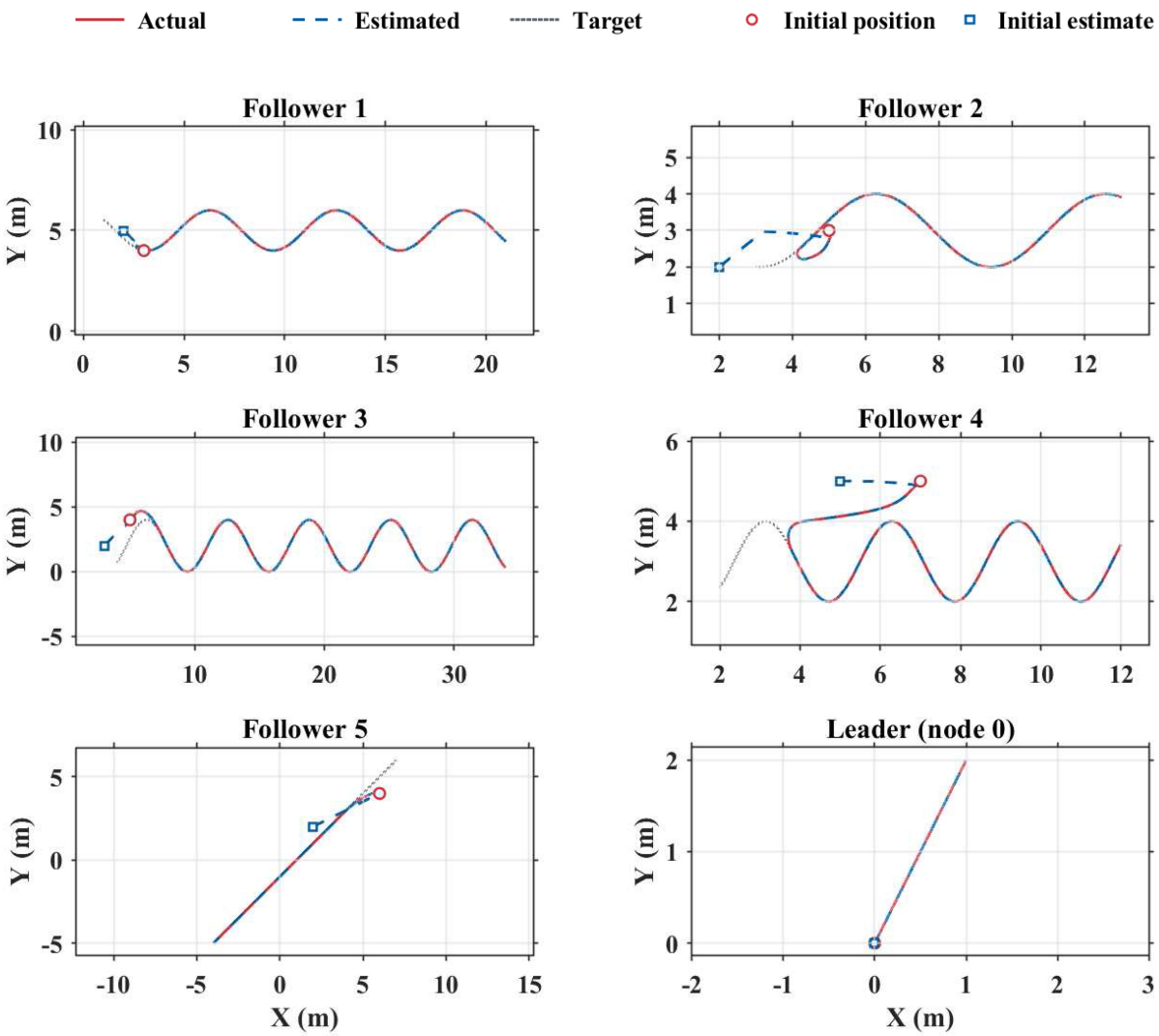

Figure 8. The estimated trajectories with common orientation and target paths.

The initial orientation values of the leader and followers are selected as

$$\theta_0(0) = 1.1071, \quad \{\theta_i(0)\}_{i=1}^{5} = \{1.5671, 4.7126, 4.7132, 4.7136, 3.9270\}. \tag{22}$$

The orientation and position gains are $\eta_2 = 5$ and $\eta_3 = 5$ for every follower. The orientation-update perturbations are uniformly distributed on [-0.01, 0.01] rad/s, and each position-update component is uniformly distributed on [-0.5, 0.5] m/s. Thus $L_i^{\theta} = 0.01$ and $L_i^{p} = 0.5$, and the gain conditions in (14) and (15) and Theorem 2 become

$$\eta_2 = 5 > L^{\theta} = 0.01, \qquad \eta_3 = 5 > L^{p} = \max_i \nu_i L_i^{p} = 0.5.$$

The initial position estimates are the same as in Scenarios 1-2. The initial orientation estimates are

$$(\hat{\theta}_i(0))_{i=1}^{5} = (\pi/8, 0, \pi/4, 0, \pi/2), \qquad \hat{\theta}_0(0) = 1.1071.$$

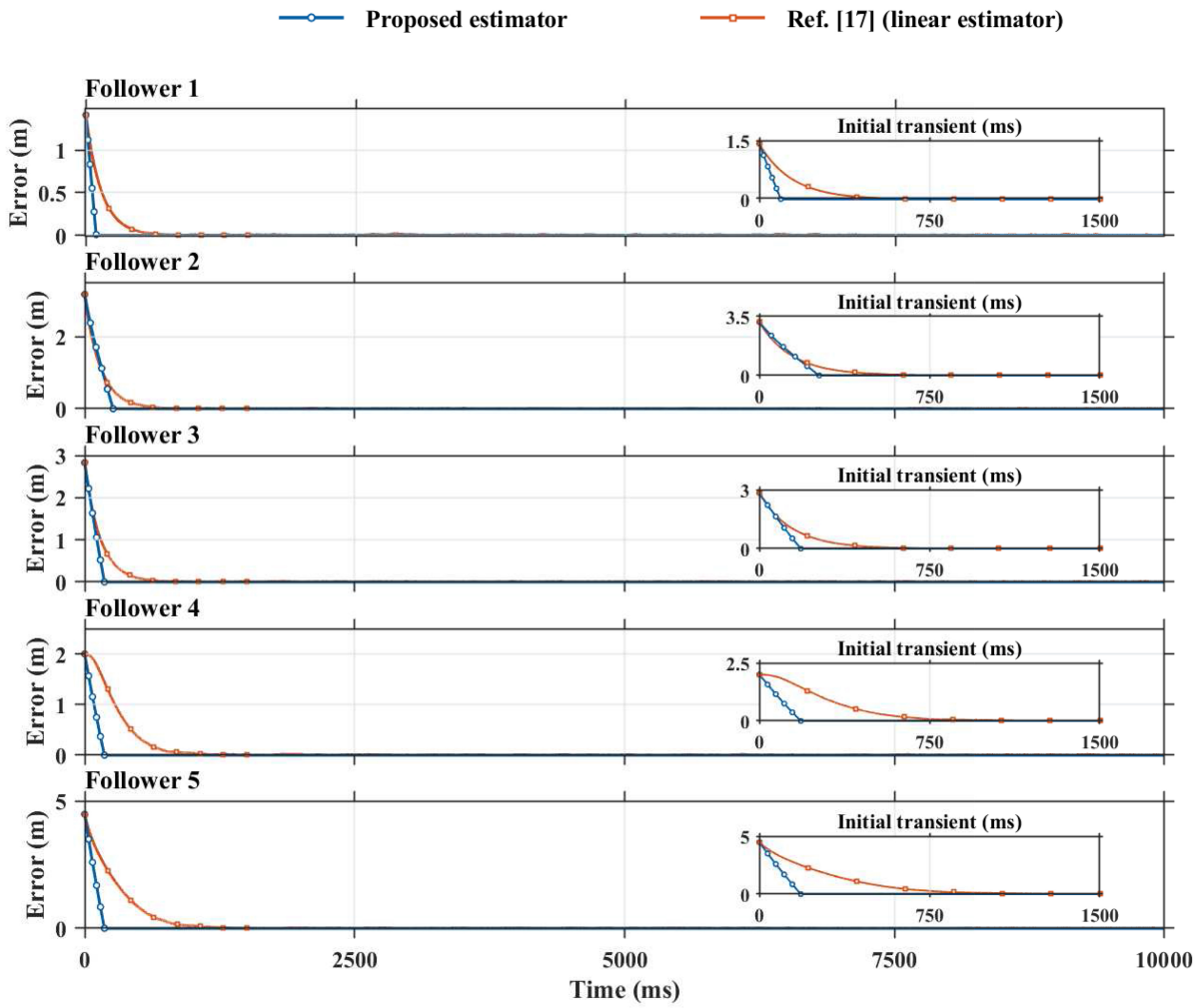

Figure 9. Position-error comparison with common orientation and moving targets. Each panel represents one follower. Blue circles: proposed estimator; orange squares: velocity-fed linear comparison based on[17]. Main panels: 0-10,000 ms; initial-transient insets: 0-1,500 ms.

The tracking gains are $(\alpha_i)_{i=1}^{5} = (6, 6, 36, 44, 8)$ and $(\beta_i)_{i=1}^{5} = (3, 3, 3, 3, 0.5)$. The tracking gains in all three scenarios satisfy $\alpha_i > \beta_i^2/2$.

The adopted controller is given below

$$u_i = -\alpha \operatorname{sgn}\left[R_{\hat{\theta}_i} v_i^i - \dot{p}_i^* + \beta \operatorname{sig}^{\frac{1}{2}}(\hat{p}_i - p_i^*)\right]. \tag{23}$$

To generate the moving local frames in Scenario 3, let θ_i^* be a continuous lift of the tangent direction $\operatorname{atan2}(\dot{p}_{i,y}^*, \dot{p}_{i,x}^*)$ of the target path. The follower angular motions are simulated by

$$\dot{\theta}_i^c = \omega_i, \qquad \dot{\omega}_i = -a_i^\omega \operatorname{sgn}\left[\omega_i - \dot{\theta}_i^* + b_i^\omega \operatorname{sig}^{1/2}(\zeta_i)\right],$$
$$\zeta_i = \operatorname{atan2}\left(\sin(\hat{\theta}_i - \theta_i^*), \cos(\hat{\theta}_i - \theta_i^*)\right),$$

with $(a_i^\omega)_{i=1}^{5} = (6, 6, 24, 12, 6)$, $(b_i^\omega)_{i=1}^{5} = (3, 3, 3, 2, 3)$, and $\omega_i(0) = 0$. The leader heading remains equal to $\theta_0(0)$.

In (23), the estimated orientation $\hat{\theta}_i$ and estimated position $\hat{p}_i$ serve as feedback information for path tracking. The controller in (23) is adopted only for evaluating the proposed localization estimation algorithm.

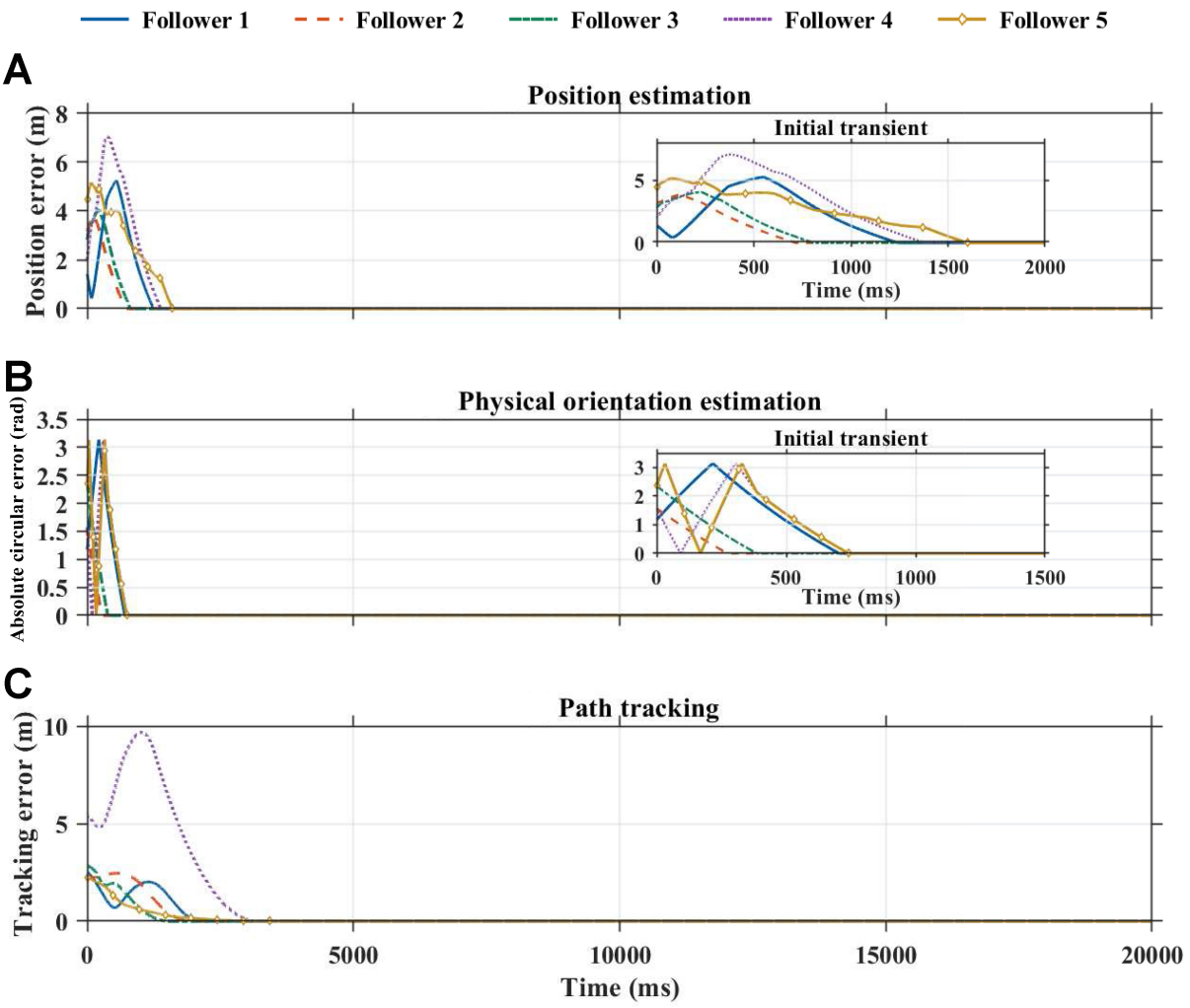

Figure 10. Moving targets without common orientation: (A) position-estimation errors in metres; (B) absolute physical circular orientation errors in radians; (C) path-tracking errors in metres. Insets resolve the initial estimation transients. Follower colours and line styles are consistent across panels; time is in milliseconds.

Figure 10 separates position estimation, physical orientation estimation, and path tracking into Figure 10A-C, respectively. The physical circular orientation error is evaluated as

$$e^{\theta}_{i,\mathrm{circ}} = \left|\mathrm{atan2}\left(\sin(\hat{\theta}_i - \theta^c_i), \cos(\hat{\theta}_i - \theta^c_i)\right)\right|.$$

Follower colours and line styles are consistent across the panels. On the saved grid, all circular orientation errors remain below 10^{-7} rad from $t = 0.743$ s, and all position errors remain below 10^{-7} m from $t = 1.601$ s. The conservative orientation settling-time bound is approximately 1.102 s. The transient position responses need not decrease monotonically while the estimated orientations are approaching their physical values. Figure 11 compares the actual and estimated trajectories. The continuous-time results establish exact finite-time convergence, while these sampled curves provide numerical evidence.

Follower 5 follows (7 - 1.1t, 6 - 1.1t) in (19) and (7 - 0.55t, 6 - 0.55t) in (21). Its target is (-4, -5) m at $t = 10$ s in Scenario 2 and at $t = 20$ s in Scenario 3; the two scenarios therefore use different target speeds.

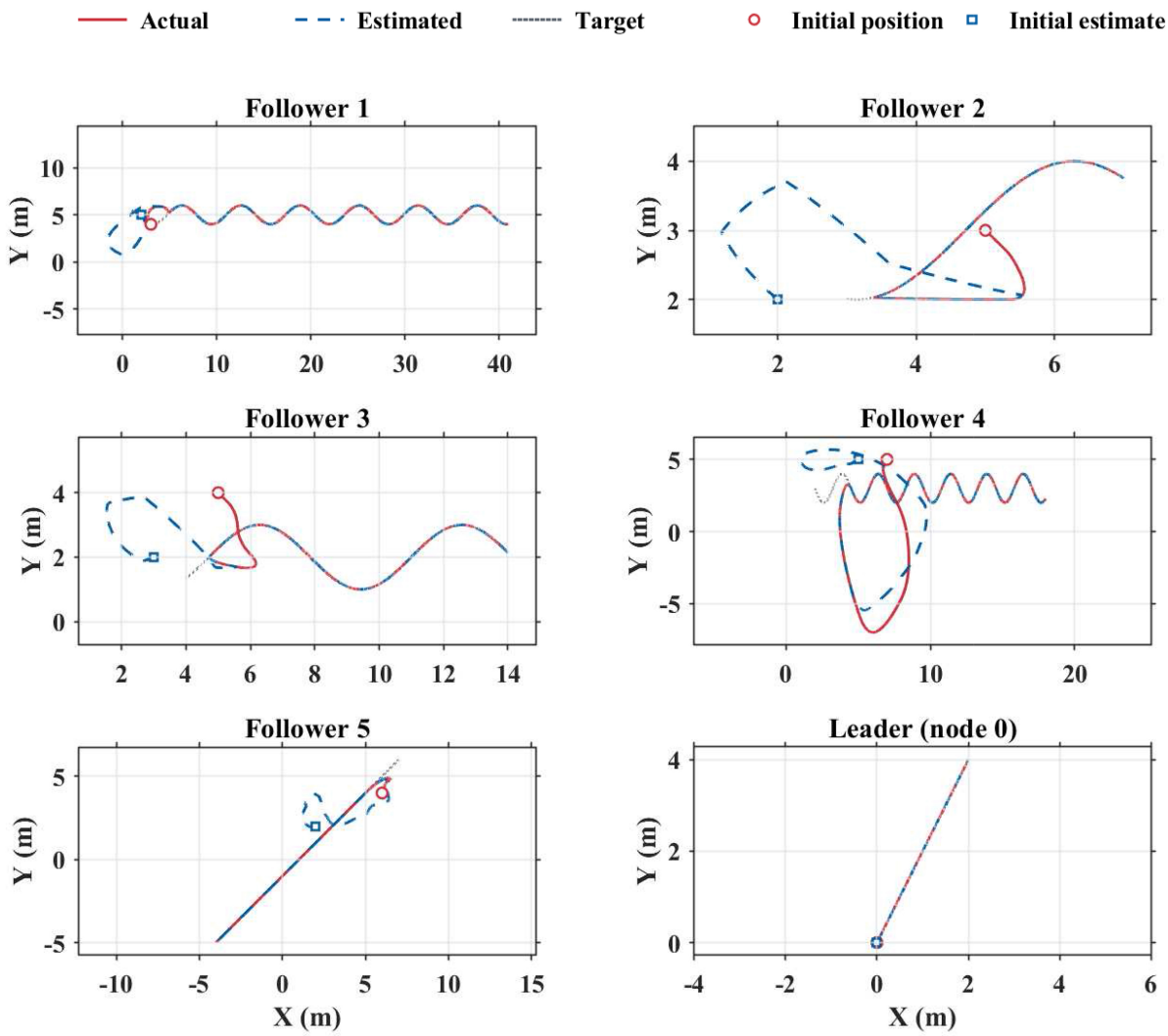

Figure 11. The estimated trajectories without common orientation.

For the comparison without common orientation, the linear estimation structures in[19] are extended to the same moving local frames used by Algorithm 2. The implemented comparison equations are

$$\dot{\check{\theta}}_i = \omega_i + k_\theta\left(\check{\theta}_{\rho(i)} - \check{\theta}_i - \bar{\theta}_{\rho(i)i}\right) + \varepsilon_i^\theta,$$
$$\dot{\check{p}}_i = R_{\check{\theta}_i} v_i^i + k_p\left(\check{p}_{\rho(i)} - \check{p}_i - R_{\check{\theta}_i} p^i_{\rho(i)i}\right) + \varepsilon_i^p,$$

with $k_\theta = 5$ and $k_p = 20$. The own angular-rate and velocity feedforward terms and the continuous tree-edge angle lifts extend the linear structure to time-varying local-frame orientations. Both observers use the same simulated motion, initial estimates, exact leader references, local measurements, integration steps, and additive perturbations. Figure 12 shows their position errors separately for each follower.

Some transient curves cross before approaching their final levels. The largest position-error peak across the followers is approximately 7.04 m for the proposed estimator and 8.82 m for the linear comparison. The proposed position errors remain below 10^{-7} m from $t = 1.601$ s. Over $2 \le t \le 20$ s, the comparison has an aggregate position-error root-mean-square value of approximately 3.04×10^{-3} m. These observations describe the localization responses for the stated gains and bounded update perturbations.

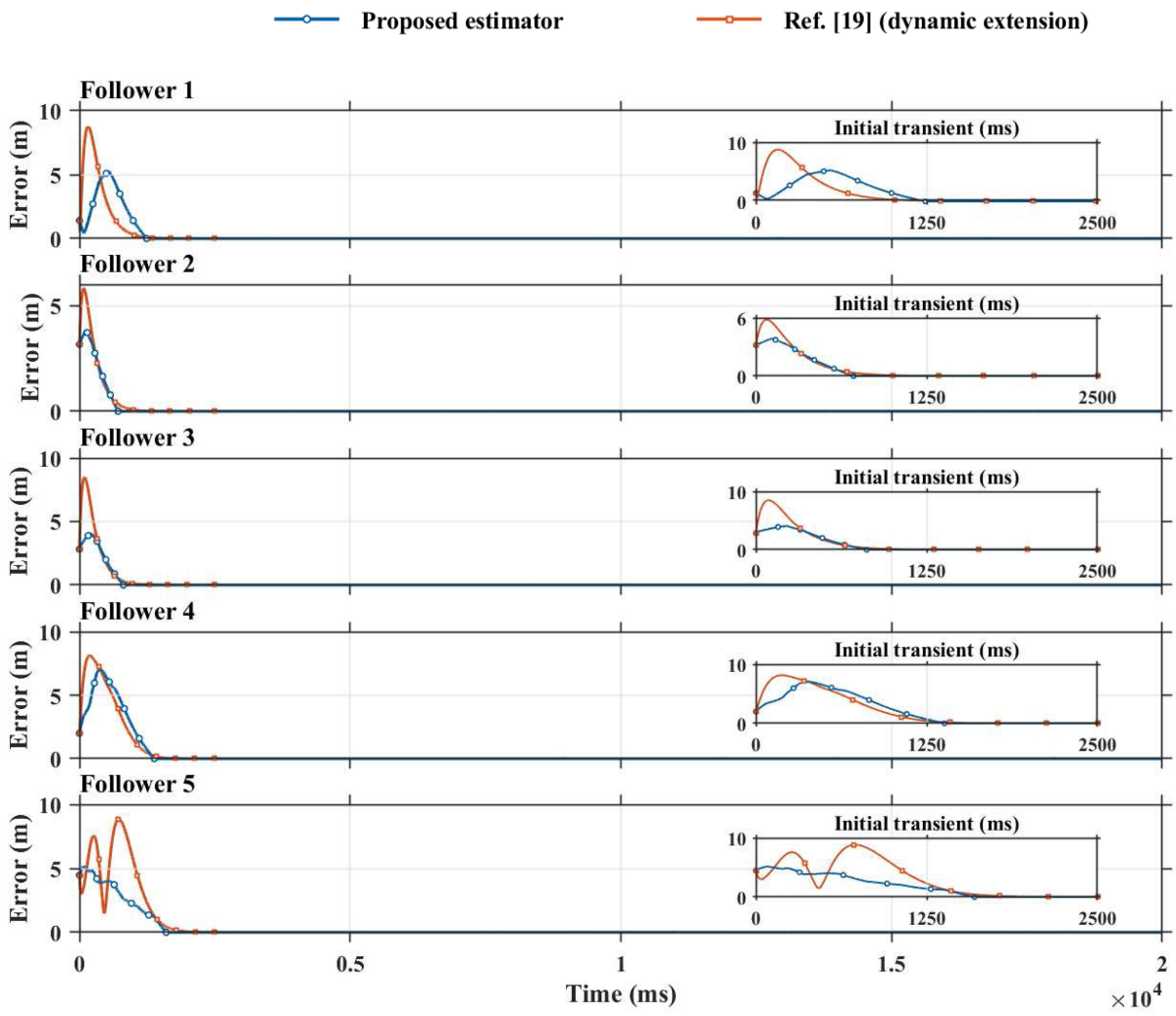

Figure 12. Position-error comparison without common orientation. Blue circles: Algorithm 2; orange squares: the specified moving-frame extension of the linear estimation structure in[19]. Each panel represents one follower. Main panels: 0-20,000 ms; initial-transient insets: 0-2,500 ms.

4.1.4. Continuous-angle representation and ideal-measurement validation

The continuous-angle representation and the estimators (14) and (15) are evaluated with exact measurements using one leader and five followers, while the associated wrapped relative angles cross their branch boundaries. The simulation duration is 12 s, with gains $\eta_2 = 3$ and $\eta_3 = 4$. Local measurements are exact and available without delay, and the update perturbations are $\varepsilon_i^{\theta} = 0$ and $\varepsilon_i^{p} = 0$. The disturbance magnitudes are zero, so the gains $\eta_2 = 3 > 0$ and $\eta_3 = 4 > 0$ satisfy the corresponding gain conditions of Theorem 2.

The position-estimation neighbor sets are $\mathcal{N}_1 = \{0, 2\}$, $\mathcal{N}_2 = \{1, 3\}$, $\mathcal{N}_3 = \{1, 5\}$, $\mathcal{N}_4 = \{2, 5\}$, and $\mathcal{N}_5 = \{3, 4\}$, where node 0 denotes the leader. The orientation estimator uses a leader-rooted tree with $\rho(1) = 0$, $\rho(2) = \rho(3) = 1$, $\rho(4) = 2$, and $\rho(5) = 3$, whereas the position estimator uses all the listed edges.

The initial follower positions are given by $\mathcal{P}_0$ in (21), and the initial true headings are specified in (22). The prescribed motions are

$$p_0(t) = (0.1t, 0.2t)^{\mathsf{T}},$$
$$p_i(t) = p_0(t) + p_i(0) + \left(a_i^x \sin(\kappa_i t),\ a_i^y [\cos(\kappa_i t) - 1]\right)^{\mathsf{T}}, \quad i = 1, \ldots, 5,$$

where the amplitudes, frequencies, and angular velocities are specified by

$$(a_i^x)_{i=1}^5 = (0.20, 0.18, 0.15, 0.22, 0.17)\ \mathrm{m},$$
$$(a_i^y)_{i=1}^5 = (0.18, 0.20, 0.16, 0.19, 0.15)\ \mathrm{m},$$
$$(\kappa_i)_{i=1}^5 = (0.40, 0.55, 0.65, 0.50, 0.70)\ \mathrm{s}^{-1},$$
$$(\omega_i)_{i=0}^5 = (0.15, -0.45, 0.35, -0.20, -0.55, 0.65)\ \mathrm{rad/s}.$$

The headings evolve as $\theta_i^c(t) = \theta_i(0) + \omega_i t$ for $i = 0, \ldots, 5$.

The initial follower position estimates are {(2,5), (2,2), (3,2), (5,5), (2,2)} m, and the initial orientation estimates are (0.4, -1.3, 2.7, 0.8, -2.2) rad. The leader provides its exact reference data. Each tree-edge lift is initialized from reciprocal local bearings using (13) and subsequently propagated by the angular-velocity difference. The estimators are integrated by implicit Euler with step size $h = 10^{-3}$ s, using componentwise soft thresholding to solve the implicit set-valued sign terms.

Figure 13A shows two branch crossings at approximately 0.77 and 11.24 s. The wrapped relative angle jumps between 0 and 2π, while the lifted angle remains continuous. Figure 13B presents the circular orientation error $e_{i,\mathrm{circ}}{}^{\theta} = |\mathrm{atan2}(\sin(\hat{\theta}_i - \theta_i^c), \cos(\hat{\theta}_i - \theta_i^c))|$, and Figure 13C shows the position error $||\hat{p}_i - p_i||_2$. Both errors approach zero within approximately 2 s and remain small during the subsequent branch crossing. The corresponding theoretical orientation settling-time bound is $\max_i|q_i(0)|/\eta_2 \approx 2.7941$ s. The insets in Figure 13B and C resolve the main error transients over 0-2 s, while the complete records show the small errors through the later branch crossing. Matching follower styles identify the corresponding orientation and position responses. The wrapped-angle jumps in Figure 13A do not enter the orientation feedback after initialization. The results demonstrate continuity of the integrated angle representation and orientation recovery modulo 2π, followed by position recovery, under exact angular velocities. This case addresses the ideal-measurement model of Theorem 2; the effects of angular-rate bias are described in Remark 4.

The initial headings are not contained in a common interval of length less than π. Successful localization in this case also illustrates the applicability of the estimators beyond this initial-orientation restriction.

4.2. Experiment

Localization results obtained from recorded QBot-2e robot data are presented in this subsection, with the experimental platform shown in Figure 14A. Each robot communicates with Matlab/Simulink through the QUARC real-time control software. The lidar sensor provides the relative distance and bearing angle between robots, where the distance information is also used for collision avoidance. The relative positions are obtained by combining lidar-based bearing angles with odometry data from wheel encoders and the robot kinematic model, and the relative velocities are then computed from the relative positions. The angular velocities are obtained from wheel-encoder measurements using the differential-drive kinematics of the QBot-2e robots. The estimator reads these values from the Twist.Twist.Angular.Z field of each robot's record_odom messages. The SLAM technique provides the ground-truth global position of each robot for performance evaluation. The employed laser radar is the SLAMTEC RPLIDAR A2M8, with an angular resolution of 0.45° and a specified ranging distance of 0.2-12 m. More information is available at https://www.slamtec.com/cn/Lidar/A2Spec.

In the experimental setup, an external computer processes the graph-constrained localization updates, while the robots provide measurements and execute the received commands. The data collected from each robot are transmitted to the computer and processed according to the distributed localization scheme. For example, the update term $\dot{\hat{p}}_i$ is computed from the information of robot i and its neighbors. Thus, the experiment preserves the distributed information structure of the proposed algorithm. Although lidar is used

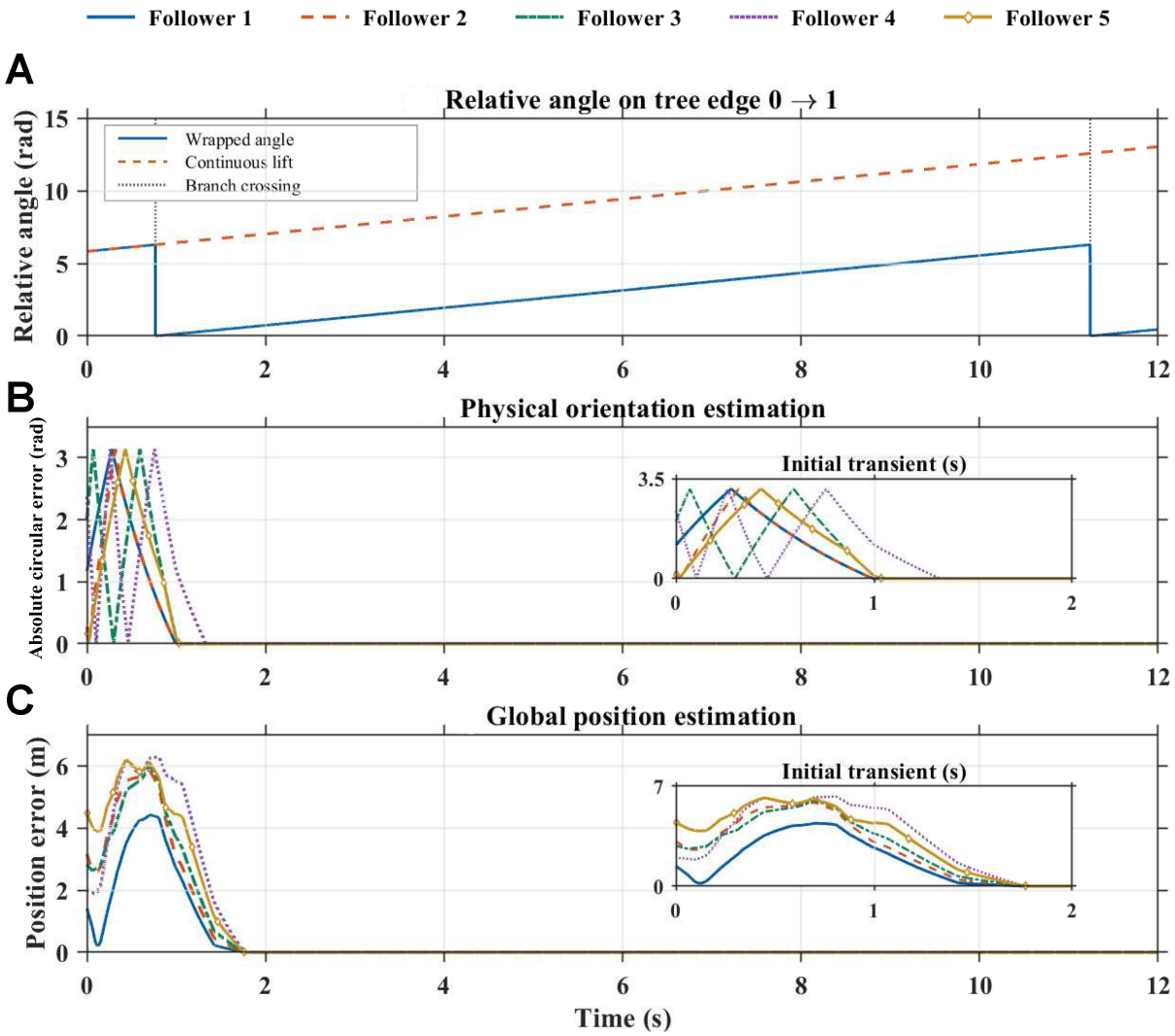

Figure 13. Continuous-angle representation and localization under exact measurements: (A) wrapped and continuously lifted relative angles on tree edge 0 ⟶ 1; (B) absolute circular orientation estimation errors; (C) position estimation errors. The insets in (B) and (C) enlarge 0-2 s. Matching follower colours and line styles are used across these panels: blue solid, orange dashed, green dash-dotted, purple dotted, and gold solid with hollow diamonds for followers 1-5, respectively. The wrapped angle is a reference trace and is used for orientation initialization only. In (A), the blue solid and orange dashed curves denote the wrapped angle and its continuous lift; vertical dotted lines mark branch crossings.

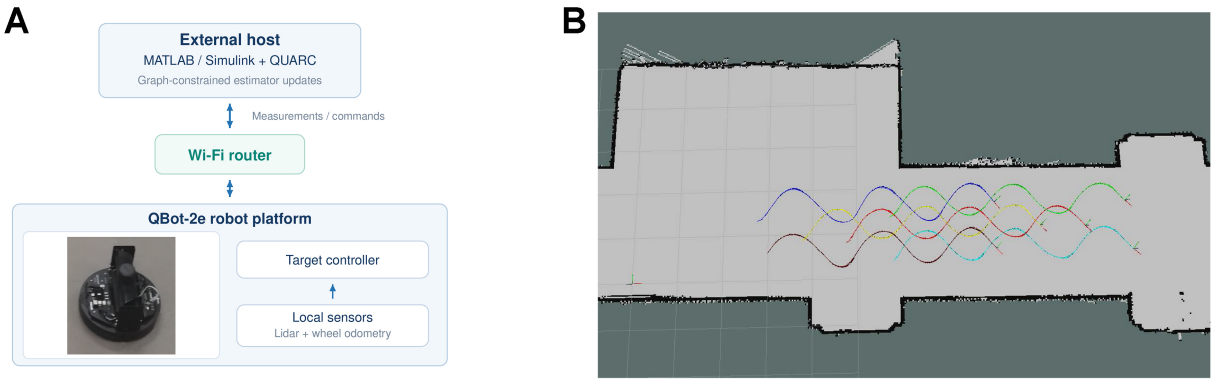

Figure 14. Experimental platform and robot trajectories: (A) experimental platform; (B) robot trajectories. The inset robot photograph in (A) was taken by the authors.

in this experiment because it is available on the robots, other low-cost sensors, such as ultra-wideband (UWB) devices and gyroscopes, can also be adopted as alternatives.

The six robots are initialized at

$$\begin{aligned}\mathcal{P}_{\exp}(0) =&\{(4.7191, 1.9515), (4.7850, 0.9640), (3.7686, 1.4644),\\ &(2.7974, 1.4788), (1.7219, 1.9508), (1.7092, 1.0155)\}.\end{aligned} \tag{24}$$

The lidar measurements of relative distance and angle already contain random noise. Therefore, no extra disturbance is introduced in this experiment.

The recorded initial orientations are

$$\begin{aligned}\theta_0(0) &= -0.3208,\\ \{\theta_i(0)\}_{i=1}^{5} &= \{-0.3423, -0.3848, -0.3774, -0.4349, -0.3395\}.\end{aligned} \tag{25}$$

Each robot follows a sinusoidal trajectory, as shown in Figure 14B.

The positions in (24) are listed in the order of followers 1-5 followed by leader 0. The follower estimates are initialized as

$$\begin{aligned}\{\hat{p}_i(0)\}_{i=1}^{5} &= \{(2, 5), (2, 2), (3, 2), (5, 5), (2, 2)\}\ \mathrm{m},\\ \{\hat{\theta}_i(0)\}_{i=1}^{5} &= \{0, 0, 0, 0, 0\}\ \mathrm{rad}.\end{aligned}$$

The leader estimates are set to its recorded reference position and orientation. The resulting initial error magnitudes, in follower-index order, are

$$\begin{aligned}\left(\|\hat{p}_i(0) - p_i(0)\|_2\right)_{i=1}^{5} &= (4.0849, 2.9714, 0.9368, 4.1534, 0.2824)\ \mathrm{m},\\ \left(|\hat{\theta}_i(0) - \theta_i(0)|\right)_{i=1}^{5} &= (0.3423, 0.3848, 0.3774, 0.4349, 0.3395)\ \mathrm{rad}.\end{aligned}$$

These values agree with the initial errors in Figure 15; the initial true and estimated positions are also shown in Figure 16.

The raw six-robot recording spans approximately 96.67 s. After excluding the final 10 s, the localization dataset contains 5,200 samples over approximately 86.65 s. Its mean sampling frequency is approximately 60 Hz, corresponding to a mean sampling interval $\bar{T}_s \approx 1/60$ s ≈ 16.67 ms. Each estimator update uses the actual interval between consecutive recorded timestamps. With samples indexed by $k = 1, \ldots, 5{,}200$, the conversion to elapsed time is

$$t_k - t_1 = \sum_{\ell=2}^{k} (t_\ell - t_{\ell-1}) \approx (k-1)\bar{T}_s.$$

Figures 15 and 17 use the same raw measurements from this six-robot recording, with separately saved estimation outputs. Figure 15 displays samples 1-1,500, approximately 24.98 s, whereas Figure 17 displays samples 1-2,000, approximately 33.32 s. Both horizontal axes use the sample index and the same time conversion; the displayed intervals have different lengths.

The relative headings reconstructed from the recorded orientation data exhibit transitions across the $0/2\pi$ boundary when represented in $[0, 2\pi)$. Figures 15-17 use a sampled heading-feedback implementation rather than the complete continuous-lift Algorithm 2. Let $j = \rho(i)$ and $h_k = t_{k+1} - t_k$. At sample k, the current recorded parent–child heading difference is defined as

$$\theta_{ji}^{\mathrm{rec}}[k] = \operatorname{atan2}\left(\sin\left(\theta_j^{\mathrm{rec}}[k] - \theta_i^{\mathrm{rec}}[k]\right), \cos\left(\theta_j^{\mathrm{rec}}[k] - \theta_i^{\mathrm{rec}}[k]\right)\right).$$

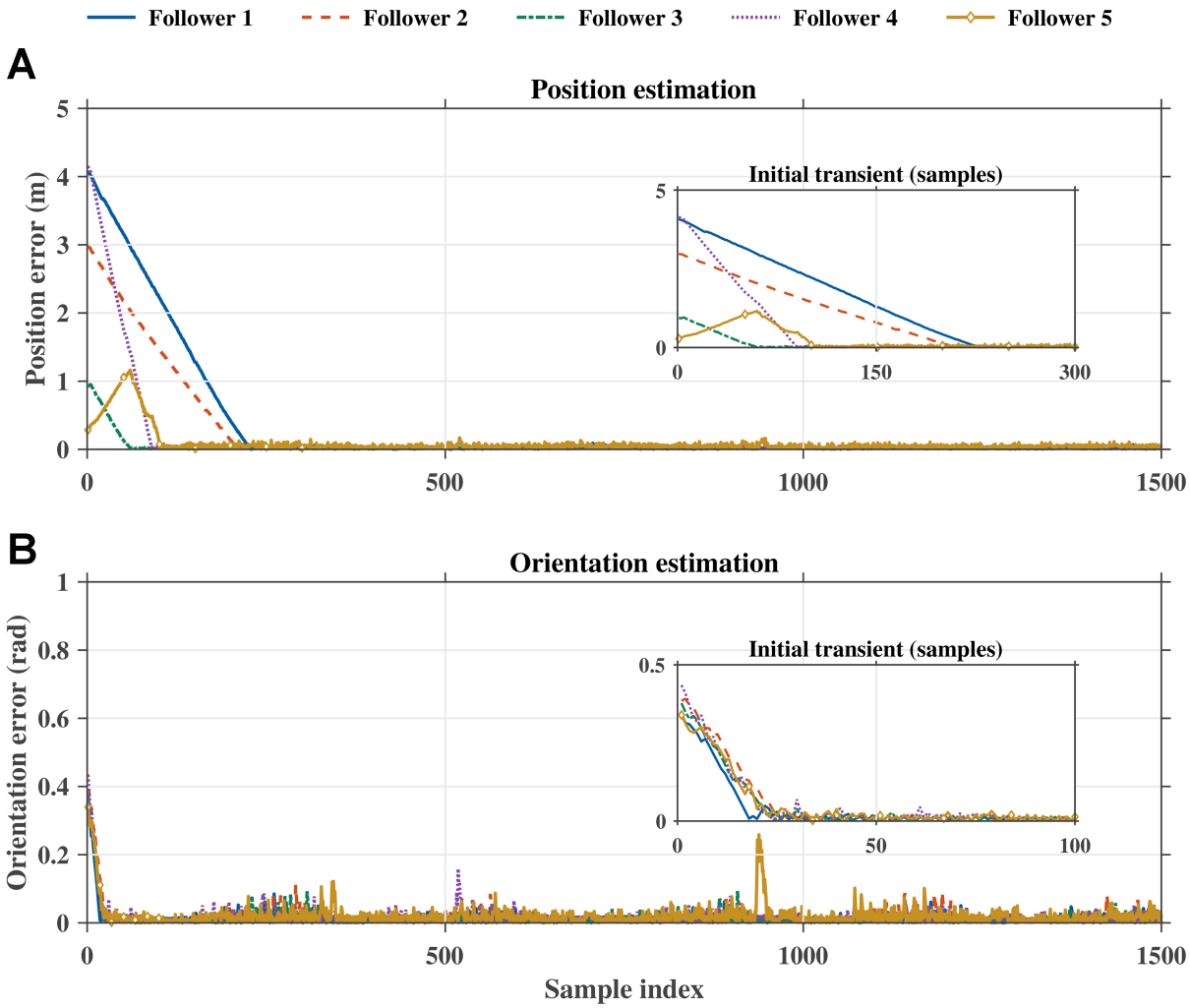

Figure 15. Experimental position and orientation estimation errors without common orientation: (A) position errors in metres; (B) orientation errors in radians. The insets enlarge the first 300 and 100 samples, respectively. Matching colours and line styles identify followers 1-5 across the two panels. The horizontal axes use the sample index.

The corresponding circular orientation-feedback residual is

$$r_i^{\theta}[k] = \operatorname{atan2}\left(\sin\left(\hat{\theta}_j[k] - \hat{\theta}_i[k] - \theta_{ji}^{\mathrm{rec}}[k]\right), \cos\left(\hat{\theta}_j[k] - \hat{\theta}_i[k] - \theta_{ji}^{\mathrm{rec}}[k]\right)\right).$$

The sampled orientation update is

$$\hat{\theta}_i[k+1] = \hat{\theta}_i[k] + h_k\left[\dot{\hat{\theta}}_j[k] - (\omega_j[k] - \omega_i[k]) + \eta_2 \operatorname{sgn}\left(r_i^{\theta}[k]\right) + r_i^{\theta}[k]\right].$$

For the position estimator, define

$$r_i^{p}[k] = \sum_{\ell \in \mathcal{N}_i} a_{i\ell}\left(\hat{p}_\ell[k] - \hat{p}_i[k] - R_{\hat{\theta}_i[k]} p_{\ell i}^{i}[k]\right), \qquad \nu_i = \sum_{\ell \in \mathcal{N}_i} a_{i\ell}.$$

The timestamp-based sampled position update is

$$\begin{aligned}\hat{p}_i[k+1] = \hat{p}_i[k] + h_k\Bigg[&\frac{1}{\nu_i}\sum_{\ell \in \mathcal{N}_i} a_{i\ell}\dot{\hat{p}}_\ell[k] \\ &- \frac{1}{\nu_i}\sum_{\ell \in \mathcal{N}_i} a_{i\ell}\left(R_{\hat{\theta}_\ell[k]} v_\ell^{\ell}[k] - R_{\hat{\theta}_i[k]} v_i^{i}[k]\right) \\ &+ \frac{\eta_3}{\nu_i}\operatorname{sgn}\left(r_i^{p}[k]\right) + \frac{1}{\nu_i} r_i^{p}[k]\Bigg].\end{aligned}$$

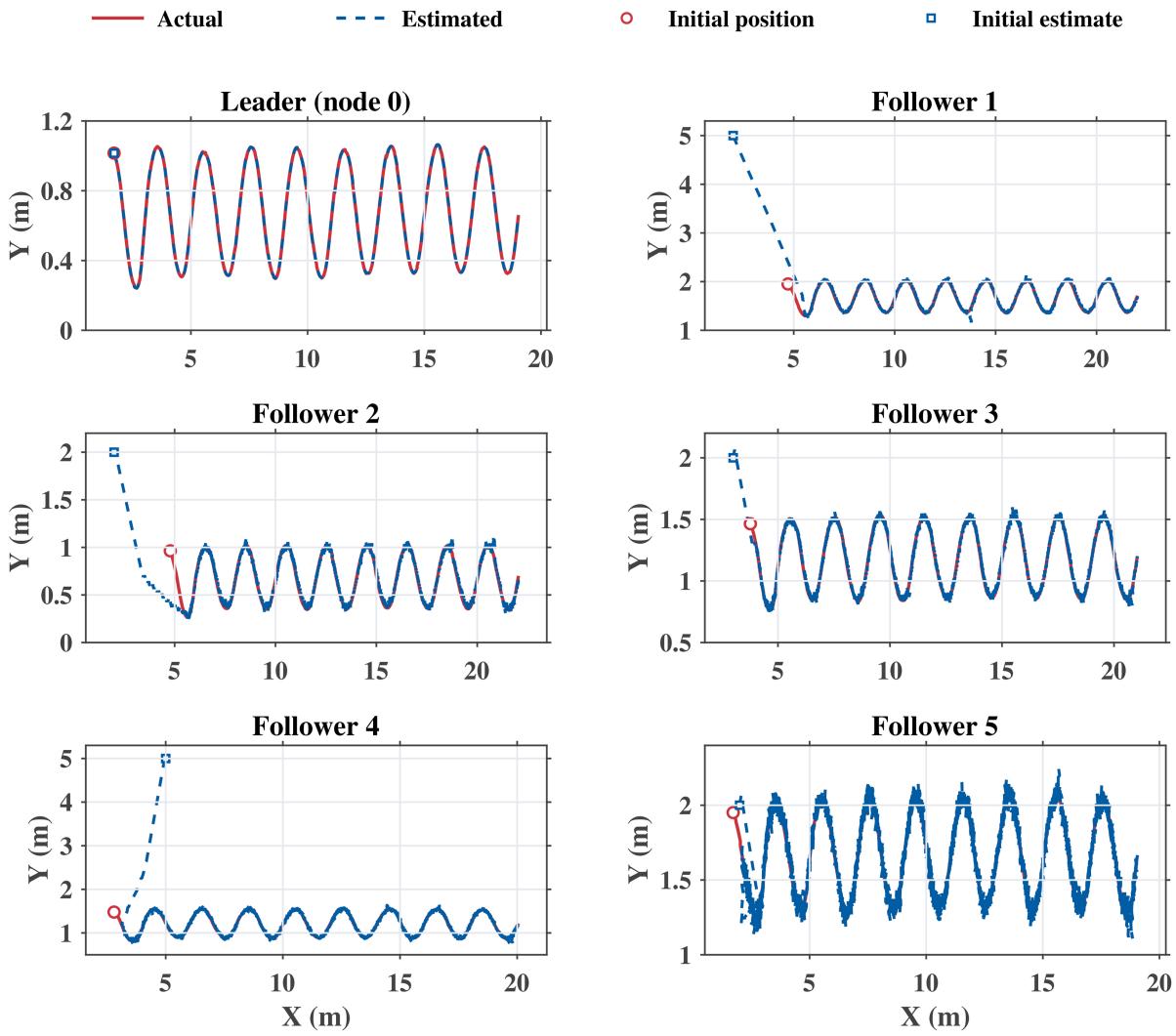

Figure 16. Robot trajectories without common orientation. Red solid and blue dashed curves denote the actual and estimated trajectories. Hollow circles and squares mark their initial positions. The panels show leader 0 and followers 1-5.

Here, $\dot{\hat{\theta}}_j[k]$ and $\dot{\hat{p}}_\ell[k]$ denote the parent and neighbor estimator update rates evaluated at sample k, respectively. The sign function in the position update is applied componentwise. No additional artificial update disturbance is introduced; measurement noise is contained in the recorded inputs.

Unlike Algorithm 2, this recorded-data implementation refreshes the relative-heading feedback at every sample instead of initializing a continuous lift once and subsequently propagating it solely through angular-rate differences. Accordingly, Figure 13 evaluates the complete continuous-lift Algorithm 2, whereas Figures 15 and 16, together with the recorded-data implementation curves in Figure 17, evaluate the sampled heading-feedback implementation using the recorded robot data.

Using the sampled heading-feedback recorded-data implementation defined above, the robot-based experimental results under the non-common-orientation case are presented in Figures 15-17. Figure 15A presents the position errors $||\hat{p}_i - p_i||_2$ in metres, and Figure 15B presents the orientation errors $|\hat{\theta}_i - \theta_i|$ in

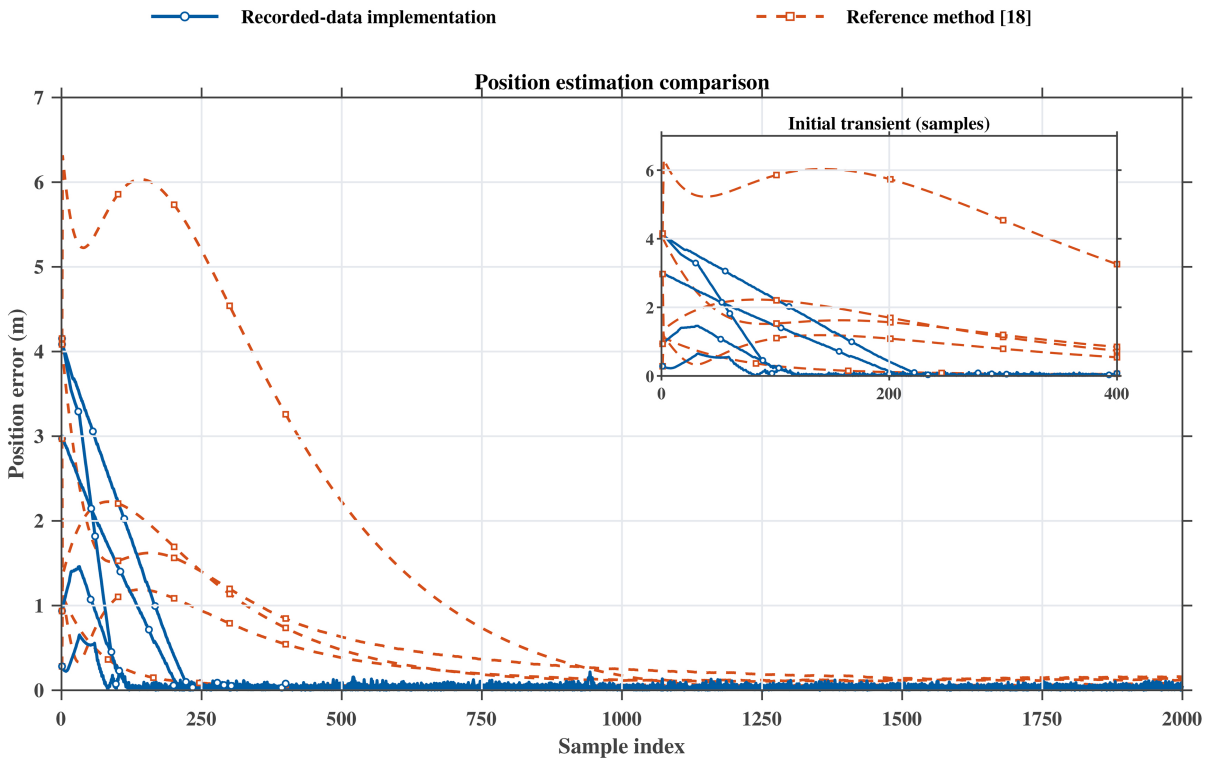

Figure 17. Comparison of position estimation errors without common orientation. Blue solid curves with hollow circles: recorded-data implementation; orange dashed curves with hollow squares: the reference method in[18]. Each group contains five traces. The main panel shows samples 1-2,000, and the inset enlarges samples 1-400.

radians. Matching colours and line styles identify the five followers in both panels. The insets resolve the first 300 position samples and the first 100 orientation samples. Both errors decrease rapidly from their initial values and subsequently remain near zero with small fluctuations under the recorded sampled measurements.

Figure 16 compares the actual red solid trajectories with the estimated blue dashed trajectories. Hollow circles and squares mark the actual and estimated initial positions, respectively. The estimated trajectories approach the recorded robot motions after the initial localization transient, with the complete saved trajectories and initial positions displayed in all six panels.

The saved estimation-error curves exhibit small fluctuations after the initial transient. The archived data-processing implementation includes no dedicated angular-rate bias estimator or periodic recalibration step, while the current heading-difference feedback provides orientation correction at each sample. These results characterize the sampled heading-feedback implementation over the recorded interval. The accumulated drift associated with continuous angular-rate propagation is quantified analytically in Remark 4.

Figure 17 presents the saved position-error comparison for the robot experiment. Blue solid curves with hollow circles show the recorded-data implementation, and orange dashed curves with hollow squares show the reference method in[18]. Each group contains five error traces. The inset enlarges the first 400 samples, while the main panel retains the complete 2,000-sample comparison interval. The blue curves display a shorter initial position-error transient in this saved run.

The simulations illustrate rapid localization with and without a common orientation reference. The exact-measurement case demonstrates continuous angle propagation and orientation and position recovery while the associated wrapped reference angles cross their branch boundaries. The robot experiments further illustrate the practical localization behavior of the sampled heading-feedback recorded-data implementation.

5. CONCLUSION

This paper addressed distributed self-localization for dynamic multi-agent systems under local perception, with particular emphasis on the absence of a common orientation reference. A distributed orientation estimator based on local relative bearing measurements with continuous angle lifts on a leader-rooted tree was developed to recover the global orientation of each follower, and the recovered orientation information was subsequently used for distributed position estimation under a leader-follower framework. The proposed framework also covers the case with a common orientation reference. Theoretical analysis established finite-time convergence of the orientation (modulo 2π) and position estimation errors under the stated exact-measurement and bounded-update-perturbation conditions. Numerical simulations evaluated the complete continuous-lift estimator, including its behavior under branch crossings, whereas multi-robot experiments using recorded data illustrated rapid localization with a sampled heading-feedback implementation.

DECLARATIONS

Authors' contributions

Conceptualization, methodology, software, formal analysis, investigation, validation, visualization, writing - original draft: Shao, D.

Methodology, formal analysis, supervision, writing - review and editing: Lv, Y.

Resources, investigation, validation, writing - review and editing: Yan, H.

Conceptualization, methodology, supervision, project administration, funding acquisition, writing - review and editing: Yang, P.

Resources, investigation, validation, writing - review and editing: Gao, S.

Availability of data and materials

The data that support the findings of this study are available from the corresponding author upon reasonable request.

AI and AI-assisted tools statement

During the preparation of this manuscript, the authors used ChatGPT (version GPT-6.1 Sol, released 2026-09-29) to assist with translation and language editing. No AI tools were used in the conception, design, or production of the graphical abstract. The authors have reviewed the final manuscript and take full responsibility for its content.

Financial support and sponsorship

This work was supported by the National Natural Science Foundation of China (62403200, 62333005, 62533002, 62503174), the Shanghai Natural Science Foundation (24ZR1416200), the Shanghai Aerospace Science and Technology Innovation Fund (Grant SAST2024-066), and the Shanghai International Science and Technology Cooperation Project (Grant 24510714000), and the China Postdoctoral Science Foundation (Grant 2026T190464).

Conflicts of interest

Yan, H. is a Section Editor for Robot Control and Navigation and a Guest Editor of the special issue "AI-Driven Autonomous Localization: Multimodal Perception, Learning, and Spatial Intelligence" in *Intelligence & Robotics*. Yan, H. was not involved in the editorial processing of this manuscript, including reviewer selection, manuscript handling, or decision-making. The other authors declare no conflicts of interest.

Ethical approval and consent to participate

Not applicable.

Consent for publication

Not applicable.

Copyright

© The Author(s) 2026.

REFERENCES

1. Liang, Z.; Zhou, W.; Wang, Y.; Yang, Y. Fixed-time prescribed performance formation control of heterogeneous UAV-USV systems under actuator faults. *Intell. Robot.* **2026**, *6*, 229-52. DOI
2. Luo, M.; An, Q.; Su, H.; Chen, Y. Unknown input observer-based consensus control of uncertain multi-agent systems under intermittent communication. *J. Frankl. Inst.* **2024**, *361*, 107351. DOI
3. Lei, Y.; Wang, Z.; Wang, X.; Li, H.; Morărescu, I. Hybrid formation control for heterogeneous uncertain linear two-time-scale systems. *Automatica* **2025**, *176*, 112267. DOI
4. Peng, Y.; Yan, H.; Rao, K.; Yang, P.; Lv, Y. Distributed model predictive control for unmanned aerial vehicles and vehicle platoon systems: a review. *Intell. Robot.* **2024**, *4*, 293-317. DOI
5. Lin, Z.; Fu, M.; Diao, Y. Distributed self localization for relative position sensing networks in 2D space. *IEEE. Trans. Signal. Process.* **2015**, *63*, 3751-61. DOI
6. Zhao, S.; Zelazo, D. Localizability and distributed protocols for bearing-based network localization in arbitrary dimensions. *Automatica* **2016**, *69*, 334-41. DOI
7. Mueller, M. W.; Hamer, M.; D'Andrea, R. Fusing ultra-wideband range measurements with accelerometers and rate gyroscopes for quadrocopter state estimation. In *2015 IEEE International Conference on Robotics and Automation (ICRA)*, Seattle, USA. May 26-30, 2015. IEEE; 2015. pp. 1730-6. DOI
8. Lü, J.; Ze, K.; Yue, S.; Liu, K.; Wang, W.; Sun, G. Concurrent-learning based relative localization in shape formation of robot swarms. *IEEE. Trans. Autom. Sci. Eng.* **2025**, *22*, 11188-204. DOI
9. Cao, Y.; Beltrame, G. VIR-SLAM: visual, inertial, and ranging SLAM for single and multi-robot systems. *Auton. Robot.* **2021**, *45*, 905-17. DOI
10. Xu, H.; Wang, L.; Zhang, Y.; Qiu, K.; Shen, S. Decentralized visual-inertial-UWB fusion for relative state estimation of aerial swarm. In *2020 IEEE International Conference on Robotics and Automation (ICRA)*, Paris, France. May 31 - Aug 31, 2020. IEEE; 2020. pp. 8776-82. DOI
11. Khan, U.; Kar, S.; Moura, J. Distributed sensor localization in random environments using minimal number of anchor nodes. *IEEE. Trans. Signal. Process.* **2009**, *57*, 2000-16. DOI
12. Diao, Y.; Lin, Z.; Fu, M. A barycentric coordinate based distributed localization algorithm for sensor networks. *IEEE. Trans. Signal. Process.* **2014**, *62*, 4760-71. DOI
13. Lin, C.; Lin, Z.; Zheng, R.; Yan, G.; Mao, G. Distributed source localization of multi-agent systems with bearing angle measurements. *IEEE. Trans. Autom. Control.* **2016**, *61*, 1105-10. DOI
14. Lin, C.; Chai, G.; Lin, Z.; Yan, G.; Mao, G. Bearing angle based cooperative source localization. In *53rd IEEE Conference on Decision and Control*, Los Angeles, USA. Dec 15-17, 2014. IEEE; 2014. pp. 5387-92. DOI
15. Deghat, M.; Shames, I.; Anderson, B. D. O.; Yu, C. Localization and circumnavigation of a slowly moving target using bearing measurements. *IEEE. Trans. Autom. Control.* **2014**, *59*, 2182-8. DOI
16. Deghat, M.; Xia, L.; Anderson, B. D. O.; Hong, Y. Multi-target localization and circumnavigation by a single agent using bearing measurements: *Int J Robust Nonlinear Control* 2015;25:2362-74. DOI
17. Oh, K.; Ahn, H. Formation control of mobile agents based on distributed position estimation. *IEEE. Trans. Autom. Control.* **2013**, *58*, 737-42. DOI
18. Lee, B.; Ahn, H. Distributed formation control via global orientation estimation. *Automatica* **2016**, *73*, 125-9. DOI
19. Oh, K.; Ahn, H. Formation control and network localization via orientation alignment. *IEEE. Trans. Autom. Control.* **2014**, *59*, 540-5. DOI
20. Van Tran, Q.; Trinh, M. H.; Zelazo, D.; Mukherjee, D.; Ahn, H. Finite-time bearing-only formation control via distributed global orientation estimation. *IEEE. Trans. Control. Netw. Syst.* **2019**, *6*, 702-12. DOI
21. Zhao, Y.; Duan, Z.; Wen, G.; Zhang, Y. Distributed finite-time tracking control for multi-agent systems: an observer-based approach. *Syst. Control. Lett.* **2013**, *62*, 22-8. DOI
22. Feng, Z.; Hu, G.; Sun, Y.; Bo Woon Soon, J. Finite-time task-space coordinated tracking of networked robotic manipulators with uncertain dynamics and disturbances. *IEEE. Trans. Control. Netw. Syst.* **2021**, *8*, 1513-27. DOI
23. Cortes, J. Discontinuous dynamical systems. *IEEE. Control. Syst. Mag.* **2008**, *28*, 36-73. DOI

24. Ou, M.; Du, H.; Li, S. Finite-time formation control of multiple nonholonomic mobile robots. *Int. J. Robust. Nonlinear. Control.* **2014**, *24*, 140-65. DOI

25. Bhat, S. P.; Bernstein, D. S. Finite-time stability of continuous autonomous systems. *SIAM. J. Control. Optim.* **2000**, *38*, 751-66. DOI

Disclaimer/Publisher's Note: All statements, opinions, and data contained in this publication are solely those of the individual author(s) and contributor(s) and do not necessarily reflect those of OAE and/or the editor(s). OAE and/or the editor(s) disclaim any responsibility for harm to persons or property resulting from the use of any ideas, methods, instructions, or products mentioned in the content.



© The Author(s) 2026. Open Access This article is licensed under a Creative Commons Attribution 4.0 International License (https://creativecommons.org/licenses/by/4.0/), which permits unrestricted use, sharing, adaptation, distribution and reproduction in any medium or format, for any purpose, even commercially, as long as you give appropriate credit to the original author(s) and the source, provide a link to the Creative Commons license, and indicate if changes were made.